NTNU
Norwegian University of
Science and Technology

Optical coatings for enhancement of the longitudinal Magneto-optic Kerr Effect from magnetic ultra-thin films

Erlend Grytli Tveten

Nanotechnology
Submission date: June 2011
Supervisor: Ursula Gibson, IFY

Norwegian University of Science and Technology
Department of Physics

Optical coatings for enhancement of the longitudinal magneto-optic Kerr effect from magnetic ultra-thin films

Master's Thesis
by

Erlend Grytli Tveten

NTNU – Trondheim
Norwegian University of
Science and Technology

Department of Physics,
The Norwegian University of Science and Technology

Academic advisor: Professor Ursula J. Gibson

June 27, 2011

Declaration of independent work

I hereby declare that the work in this project has been performed independently and in accordance with the examination regulations of the Norwegian University of Science and Technology (NTNU).

Except where specified, all figures and graphics were produced using Matlab© or the Open Source vector graphics editor Inkscape. Typesetting was done using pdfTeX, Version 3.1415926-1.40.11 (TeX Live 2010).

Erlend Grytli Tveten

Preface

This thesis is written for the degree of Master of Science at the Norwegian University of Science and Technology, concluding five years of study under the program Master of Nanotechnology, with specialization within nanoelectronics. The thesis is submitted to the Department of Physics at the Faculty of Science and Technology, and is the final product for the course TFY4905 - Nanotechnology, Master's thesis. It represents independent project work over a period of 21 weeks, and is rewarded with 30 ECTS points.

I would like to thank Professor Ursula J. Gibson for great help with the theory, the experimental setup, and for general discussions around the physical concepts of the longitudinal magneto-optic Kerr effect. Her help has been invaluable during the time I've been working with this project. Furthermore I would like to thank Tor Ingve Aamodt for teaching me how to use the deposition system for producing the samples used in the experimental part of this thesis. Last I would like to thank Sigmund Ø. Størset for great help in doing AFM measurements of the thickness of permalloy thin films.

Abstract

The effect of optical coatings on the longitudinal magneto-optic Kerr effect response from 10 nm thin films of permalloy ($Ni_{84}Fe_{16}$) has been studied. Enhancement of the magneto-optic Kerr effect signal contrast of a factor 1.76 has been observed for P-polarized incident light on a trilayer configuration of aluminium, magnesium fluoride, and permalloy. A quadrilayer structure where the trilayer is overcoated with zinc sulphide enhances the signal contrast by a factor 4.05 for P-polarized light. The enhancement is also observed for S-polarized light, and is shown to be reproducible using nickel as the magnetic material and gold instead of aluminium.

The experimental data are compared to a simplified theoretical model where the electric field components are calculated using a 4 x 4 matrix algorithm. The model is found to be inadequate in predicting the longitudinal magneto-optic Kerr effect response from complex multilayer structures. This is believed to be due to a simplification in the model disregarding the phase factors of the different components reflected off the multilayered samples.

Contents

Chapter 1

Introduction

1.1 Motivation and purpose

Research on magnetic thin films and nanostructures has seen a lot of interest during the last decade due to their potential use in devices which utilize the electron's spin in switching dynamics [1, 2]. One field under investigation related to research on magnetic devices is the study of magnetic domain wall motion [3]. The domain wall is the region of a magnetic material over which the magnetization changes direction. To be able to manufacture reliable magnetic devices it is crucial to be able to observe and control the motion of the domain wall.

For the study of these magnetic structures, the *magneto-optic Kerr effect* (MOKE) magnetometry is an important experimental tool which is non-destructive and easy to implement. The technique is based on the fact that light reflected off a magnetic material changes its polarization on reflection [4]. In the *longitudinal* geometry MOKE magnetometry is sensitive to the in-plane magnetization direction, which makes it suitable for studies of ultra-thin magnetic films.

The possibility of downscaling is an important property of modern magnetic devices, and both size and shape affect the behaviour of the magnetic nanoelements [5]. Ultra-thin magnetic films are needed to keep the structure of the domain wall simple, but with downscaling comes also a decrease in the magnetic signal which is detectable using MOKE. Hence the ability to extract the maximum amount of signal from smaller magnetic structures is believed to be increasingly important in the near future. Optical coatings have been shown to be useful for enhancing the longitudinal MOKE signal from magnetic thin films [6, 7], opening up the possibility of studying smaller magnetic structures, and even observing magnetic switching dynamics using MOKE [8, 9].

1.2 Description

This thesis describes the use of optical coatings to enhance the longitudinal MOKE signal from ultra-thin films of $Ni_{84}Fe_{16}$, frequently called *permalloy*. Trilayered and quadrilayered samples have been fabricated in a vacuum deposition system, and subsequently analyzed in a NanoMOKE^{TM}2 magnetometer manufactured by Durham Magneto Optics Ltd[1].

The optical response of the trilayered and quadrilayered stacks are modelled using Abdulhalim's [10, 11] 4 x 4 matrix algorithm to calculate the amplitude reflection components. The results are used to give a theoretical prediction of the longitudinal MOKE *signal contrast* $\Delta I/I_{av}$ through a simplified model defined by Allwood et al. [12].

The model is implemented through a Matlab© routine similar to the one used by Cantwell et al. [6] and Gibson et al. [7]. The routine was inherited from Cantwell [13], and modified to account for trilayered and quadrilayered stacks with an arbitrary sequence of dielectric, metal, and magnetic layers. Though not presented in detail, a qualitative description of the modelling routine together with important modelling results are presented in Chapter 3.

Experimental results are compared to theoretical modelling results, focusing on the longitudinal MOKE signal contrast $\Delta I/I_{av}$, as defined by Allwood. Both the addition of an anti-reflection coating in the form of a dielectric overlayer, and the impact of a dielectric underlayer, have been investigated, confirming that significant signal enhancement can be achieved. Furthermore, the combination of the two, in the form of a magneto-optic layer sandwiched between two dielectric coatings, is predicted to give a stronger enhancement of the longitudinal MOKE signal contrast than any other previously published results. This prediction is also confirmed by experimental results.

The problems and error sources associated with a longitudinal MOKE experiment, especially when studying complex multilayered structures with dielectric coatings, are discussed in detail. Deficiencies in the theoretical description are exposed, and the model is found to give an inadequate description of the experimental reality when complex combinations of dielectric coatings are applied to the magnetic multilayer structure.

[1] http://www.durhammagnetooptics.com

1.3 Background

The use of magnetic memory for non-volatile storage applications was proposed by Chen et al. already in 1968 [14], and the technology was implemented with success in the magneto-optical recording discs (MO discs), first put into practical use in 1988 [15]. The storage media found widespread commercial success throughout the 90's and early 00's, though has mostly been replaced by other technologies at the time of writing. The readout mechanism of MO discs, where opposite magnetization vectors in the magnetic medium define logical 0 and 1, is based on the polar Kerr effect, where the vertical magnetization in the storage medium rotates the polarization plane of a laser beam reflected at normal incidence [16].

While modern magnetic memory devices, like magnetic random access memory (MRAM) [17], do not rely on optical readout, there is also increasing interest in magnetic devices for use in active logic elements [18, 19]. Hence, the magneto-optic Kerr effect magnetometry is still an invaluable tool in the research for future magnetoelectronics components. MOKE is extensively used as a method to study magnetic thin films and nanostructures due to its speed and inherent simplicity [12], and is also used as a quality control method in the fabrication of magnetic disks because of its non-destructive nature [20]. A simple MOKE setup in its most basic form includes only a laser beam setup, an electromagnet, a polarization analyzer, and a photodetector.

The direction of the magnetization vector in the magnetic material can be directly linked to the rotation of the polarization plane observed in the reflected light. As a consequence a mapping of the magnetic orientation on a substrate is possible by a simple surface scan with a laser beam. This constitutes the basic operational mechanism of a *Kerr microscope* [21], a popular experimental tool for investigating magnetic microstructures. Though the resolution of a conventional Kerr microscope is fundamentally limited by the wavelength of light, scanning near-field Kerr microscopes, for Kerr analysis in the submicrometre regime, have also been proposed and tested [22, 23].

1.3.1 The longitudinal magneto-optic Kerr effect

There are three different possible MOKE geometries, depending on the direction of magnetization within the magnetic medium with respect to the plane of incidence of the incoming electromagnetic wave [4]. These are the *polar*, *longitudinal*, and *transverse* geometries. Their differences are thoroughly discussed in Sec. 2.3. Polar MOKE, where the magnetization vector is oriented perpendicular to the surface of

the substrate, has by far seen the most widespread use, mainly for magneto-optical storage applications, though is not suitable for studying ultra-thin magnetic films.

Whereas polar MOKE originates from magnetic domains with magnetization vector oriented perpendicular to the surface, longitudinal and transverse MOKE arise from magnetic domains with in-plane magnetization vectors parallel to the surface. This magnetic structure is generally found in ultra-thin films due to shape anisotropy, making these techniques especially suitable for magnetic thin film research.

1.3.2 The MOKE signal contrast

There is an inherent difficulty with measuring the magnetically rotated signal from polarized laser light reflected off a magnetic thin film: The intensity of the rotated *Kerr* component of the reflected light is very small compared to the unrotated *Fresnel* reflectivity. The intensity of the Kerr signal is typically six orders of magnitude lower than the intensity of the unrotated light, making the Kerr angle close to impossible to directly measure.

In a MOKE magnetometer setup, this difficulty is circumvented by mixing in some of the unrotated Fresnel component with the rotated light. Significant contrast is achieved by analyzing the cross-terms of the Fresnel and Kerr components in the measured intensity, while rapidly changing the orientation of the magnetization in the sample. The Kerr rotation angle can then be extracted from the resulting hysteresis curve [4].

Some groups promote the ratio of the amplitudes of the Kerr and Fresnel components, the complex Kerr rotation angle Θ_k (see Sec. 2.3.3), as the figure of merit when analyzing optical rotation from thin films [24, 25], and extensive theory has been developed focusing on analytical expressions for modelling the Kerr rotation [26]. One may argue that a larger Kerr rotation means enhanced rotation effects in the magneto-optic layer. However, large Kerr rotation angles can often be a result of interference effects which minimize the Fresnel component. As such, the total signal will be small, and have a correspondingly low signal-to-noise ratio.

Following the derivation by Allwood et al. [12], it is believed that the figure of merit closest related to the signal to noise ratio is the signal contrast, $\Delta I/I_{av}$. ΔI is the difference in reflected intensity observed for opposite magnetization directions, whereas I_{av} is the average optical signal coming from the unrotated Fresnel light. The ratio of these values is a good measure of the dynamic range of the MOKE signal. Though the signal contrast is closely related to the Kerr rotation angle, it is important to note that the conditions maximizing Θ_k and $\Delta I/I_{av}$ do not in general coincide.

The minimum I_{av} observed experimentally is fundamentally limited by the amount of *depolarized* light hitting the photodetector in the experimental setup. A constant depolarization factor γ is therefore introduced to represent the contribution of general noise to the average signal. A full derivation of the expression for the MOKE signal contrast is given in Sec. 2.3.3.

1.3.3 Optical coatings

The signal-to-noise ratio of a longitudinal MOKE experiment is generally small, and much work is usually put into amplifying the Kerr rotation, and/or minimizing the background noise. A discussion of the latter was presented by Allwood et al. in 2003 [12].

However, an experimentalist is often not in position to drastically reduce the background noise arising in the experimental setup at hand. As a consequence he must amplify the signal strength to increase the signal to noise ratio. Reports on the effect of *optical coatings* on the signal contrast for longitudinal MOKE date back to 1958 [27], though significant amount of research was first conducted in the late 1980s for enhancement of the polar magneto-optic Kerr effect [28, 29], since this was the method of choice for optical readout from MO data storage media.

Optical coatings of dielectrics stacked above and/or below a magnetic thin film may enhance or worsen the MOKE signal contrast $\Delta I/I_{av}$ due to interference effects between reflections from the various interfaces in the multilayer stack. This effect has been shown to be extremely useful in the study of the polar Kerr effect from magnetic nanostructures [24]. More recently, Gibson et al. [7] used anti-reflection (AR) coatings to improve the longitudinal MOKE contrast from nanosized thin-film discs with in-plane magnetization. The mechanisms and theory behind AR coatings are further discussed in Sec. 2.1.4.

1.4 Earlier work

1.4.1 Contrast enhancement

Several groups have reported on enhancement of the polar MOKE by applying various optical coatings to magnetic thin films [24, 25, 29, 30]. The same enhancement mechanisms are present also in the longitudinal geometry, though the oblique incidence will influence the optimal multilayer configurations found. Cantwell et al. [6] describe in their article from 2006 a method for enhancing the signal contrast from longitudinal MOKE by coating a magnetic nickel thin film with a dielectric layer of

zirconium oxide (ZrO_2).

Computer modelling reveals that a dielectric layer on top of the magnetic film enhances the Kerr signal by acting like an anti-reflection coating. The method is based on matching the optical *admittance* of the magnetic thin film to that of the incident media (usually air), thereby maximizing the amount of light transmitted through to the optically active medium. Gibson et al. [7] apply the same technique to improve the longitudinal MOKE contrast from nanomagnetic structures, using zinc sulphide (ZnS) as the dielectric overcoating. The high refractive index of ZnS makes it a suitable coating for reducing the Fresnel reflection from the substrate surrounding the structures of interest.

Adding a third layer of Au on top of the overcoating dielectric is seen to further increase the computer modelled MOKE signal slightly through facilitating the admittance matching of the magnetic medium to the incident medium [13]. However, this modest increase in signal contrast is not observed experimentally.

1.4.2 Modelling techniques

Since extensive research into optical coatings for improved polar MOKE contrast was conducted in the late 1980s, increased computer power has made life easier for the experimentalist trying to model complex multilayers of optically active thin films. Several articles have been published describing computational methods for predicting the optical behaviour of multilayers of anisotropic or magneto-optic materials. The methods all have in common that they are based on matrix algebra, where each layer in the multilayer stack is characterized by its *propagation matrix*. The full optical response of the system can then easily be calculated through simple matrix multiplication of the propagation matrices associated with the different layers.

Yeh et al. [31] were among the first to develop a method for calculating the optical response from an arbitrary number of anisotropic media in a thin film multilayer stack. Their method was based on 4 x 4 matrix algebra. In 1988 Balasubramanian [28] extended the same method for calculating the reflectivity from stacks of magnetic media, focusing on optimizing the polar Kerr effect for magneto-optical storage applications. At the same time, Mansuripur [32] developed a new method, using a 2 x 2 matrix algorithm, which later spawned the development of commercial software calculating magneto-optical response based on Mansuripur's algorithm[2].

Zak et al. [33] describe a method which uses 4 x 4 matrix algorithm for calculating the propagation matrix, whereas a 2 x 2 matrix is introduced for the final calculation of the reflection components. Abdulhalim [10, 11] has later extended this

[2]http://www.mmresearch.com

4 x 4 matrix algorithm to give simplified analytical expressions for the propagation matrix of a multilayer stack of arbitrarily anisotropic or magneto-optic materials. The 4 x 4 matrix formulation of Abdulhalim is the basis of the theoretical modelling done in this thesis.

1.5 Scientific importance

1.5.1 Magnetic switching

It has already been shown that magnetic nanowires can be assembled to create a ferromagnetic NOT gate and a magnetic shift register [34], and in the later years several logic elements based on magnetic switching have been proposed [8, 19]. The possibility of combining optical readout and logic elements based on magnetism with pure magnetic switching technology is appealing, largely because of the reduction in power dissipation compared to current Si based microelectronic technology [18]. But also increased computational speed, and higher integration densities are reasons why the idea of all-magnetic logic is appealing to the computer industry and the scientific community in general.

Longitudinal MOKE is especially suited for characterizing vortex magnetization states in magnetic ring structures [35], and for this purpose optical coatings might play a vital role. Bowden et al. [36] describe a method to break the symmetry of the magneto-optic Kerr signal from mesoscale magnetic ring structures with vortex magnetization. By coating half of the ring with a dielectric, which enhances the longitudinal MOKE signal, the vortex magnetization direction can be determined by optical readout. The same group uses this technique of breaking the symmetry to construct a working all-magnetic NOT gate [9]. The possible applications of optical coatings within magneto-optical logic constructions are many, and they may be especially interesting for niche applications where low power consumption, zero powerup, and radiation hardness are important factors.

1.5.2 Outlook

The longitudinal MOKE signal is inherently weak, and is therefore not considered applicable for logics applications at this time. However, its importance in research of magnetic domain wall motion and magnetic nanostructures is already apparent. In addition, due to the enhancement techniques described in this thesis and by others, the number of possible applications of this non-destructive *in situ* magnetic domain characterization technique is expected to increase.

Following the development of more complicated coatings to enhance the longitudinal MOKE signal, the ability to accurately model the Kerr response of a multilayer stack consisting of magneto-optic, metal, and dielectric media becomes increasingly important. A better understanding of the phase factors of the signal and noise components in a MOKE experimental setup is central to make improvements on the current model used in this thesis.

Chapter 2

Theory

2.1 Light propagation in isotropic media

This chapter introduces the basic theory needed to understand the fundamentals of a longitudinal MOKE experiment. To describe the reflected optical response from a multilayer stack of magnetic, metal, and dielectric media, the theory of light propagation inside, as well as at interfaces between, isotropic media must be addressed. The theory of optical rotation observed in magnetic media is subsequently introduced and combined with the expression for reflectivity from a thin film to describe the magneto-optic Kerr effects. The starting point in the derivation is basic electromagnetic theory.

2.1.1 Maxwell's equations

Maxwell's equations for linear, isotropic media in the absence of free charges are familiarly represented as

$$\nabla \times \mathbf{H} = \frac{\partial \mathbf{D}}{\partial t} \tag{2.1}$$

$$\nabla \times \mathbf{E} = \frac{\partial \mathbf{B}}{\partial t} \tag{2.2}$$

$$\nabla \cdot \mathbf{D} = 0 \tag{2.3}$$

$$\nabla \cdot \mathbf{B} = 0 \tag{2.4}$$

where $\mathbf{H}$ and $\mathbf{E}$ are the magnetic and electric field vectors. The electric and magnetic flux densities $\mathbf{D}$ and $\mathbf{B}$ are given by the relations

$$\mathbf{D} = \epsilon\mathbf{E} \tag{2.5}$$
$$\mathbf{B} = \mu\mathbf{H} \tag{2.6}$$

where ϵ and μ are the *electric permittivity* and the *magnetic permeability* of the medium [37]. For both magnetic and non-magnetic materials at optical frequencies, μ is practically identical to the permeability of free space $\mu_0 = 4\pi \cdot 10^7$ Hm^{-1}, and will not be further addressed in this thesis. On the other hand, the electric permittivity of a medium can differ substantially from that of free space at optical frequencies. The permittivity in an isotropic medium is frequently written as

$$\epsilon = \epsilon_0(1 + \chi) \tag{2.7}$$

where $\epsilon_0 = 8.85 \cdot 10^{-12}$ Fm^{-1} is the permittivity of free space, and χ is called the *dielectric constant* of the medium. The product of the two medium constants define the speed of light in the medium as

$$c = \frac{1}{\sqrt{\epsilon\mu}} \tag{2.8}$$

whereas the *refractive index* of the medium is defined as the ratio of the speed of light in vacuum, c_0, to that in the medium:

$$n = \frac{c_0}{c} = \sqrt{\frac{\epsilon}{\epsilon_0}} = \sqrt{1 + \chi}\ . \tag{2.9}$$

Since χ can be a complex number in absorbing media, the refractive index can also be complex, and is generally described by the equation

$$N = n - ik \tag{2.10}$$

where k is known as the *absorption coefficient*. Another extremely useful quantity in thin-film optics is the *optical admittance*, defined as the ratio of the magnetic and electric field amplitudes

$$y = H/E\ . \tag{2.11}$$

In free space, y is real and often denoted as $Y = 2.654 \times 10^{-3}$ S. The optical admittance of a medium is connected to the refractive index through

$$y = N \cdot Y \text{ [38].} \tag{2.12}$$

2.1.2 The simple boundary

When an electromagnetic wave is incident on a boundary or interface between two media at an oblique angle, it is convenient to decompose the incoming wave into two orthogonal polarization states, namely the ones *perpendicular* and *parallel* to the *plane of incidence* of the incident wave. Fig. 2.1 shows a schematic image of how a boundary between two media can be represented. The incident wave is termed S-polarized, $\mathbf{E}_1^{(s)}$ (or TE for *transverse electric*), when the electric field is polarized perpendicular, and P-polarized, $\mathbf{E}_1^{(p)}$ (or TM for *transverse magnetic*), when the electric field is polarized parallel to the plane of incidence. The plane of incidence is defined as the plane spanned by the propagation vectors $\mathbf{k}$ of the incident, reflected and transmitted waves. In the remaining parts of this thesis, the S- and P-polarized components of the light will be described by a subscript, E_s and E_p, respectively.

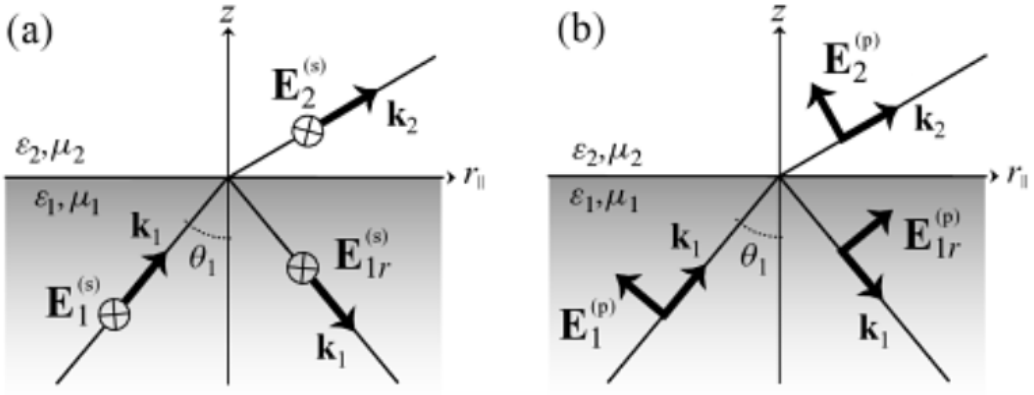

Figure 2.1: An electromagnetic wave incident on a boundary can be described either as **(a)** S-polarized, or **(b)** P-polarized, depending on the polarization state of the incident wave [39]. $\mathbf{E}$ is the electric field and $\mathbf{k}$ is the propagation vector of the incoming wave, whereas $\epsilon_{1/2}$ and $\mu_{1/2}$ are the permittivity and permeability of the two media creating the interface.

The boundary conditions for the interface are that the tangential components of the electric and magnetic fields (not shown in the figure) are continuous across the interface. These boundary conditions, together with the relation between the magnetic and electric fields in Eq. 2.11, give the familiar *Fresnel* reflection components from a single interface

$$r_s = \frac{y_1 \cos\theta_1 - y_2 \cos\theta_2}{y_1 \cos\theta_1 + y_2 \cos\theta_2} \tag{2.13}$$

$$\tag{2.14}$$

$$r_p = \frac{y_1 \cos\theta_2 - y_2 \cos\theta_1}{y_1 \cos\theta_2 + y_2 \cos\theta_1} \tag{2.15}$$

where r_s and r_p are the reflection coefficients for S-polarized and P-polarized incident light, respectively, y_1 and y_2 are the optical admittances of the two media, and θ_1 and θ_2 are the incident and transmitted angles [38].

2.1.3 Reflection and transmission from a thin film

When light is incident on a substrate coated with a thin film, two interfaces are present. Fig. 2.2 shows schematically how a light ray incident on a substrate coated with a thin film can be described[3]. The reflection and transmission from a multilayer system can be described by a simple 2 x 2 matrix algorithm, of which the most important results will be presented here.

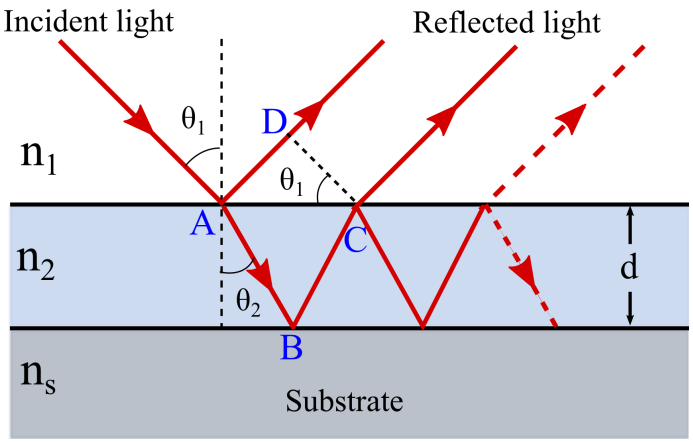

Figure 2.2: A thin film coated on top of a substrate can act as an antireflection coating provided that the optical distance travelled by the beam inside the coating material (A-B-C) equals an odd number of half wavelengths longer than the distance A-D.

[3]Except where specified by reference, schematic graphics presented in this thesis are made using the Open Source vector graphics editor Inkscape: inkscape.org.

The boundary conditions for the situation presented in Fig. 2.2 are that the tangential components of both the electric (**E**) and the magnetic ($\mathbf{H} = B/\mu$) fields be continuous across the boundaries between media 1 and 2, and media 2 and the substrate (See [40] for details). In matrix notation, this can be expressed as a relation between the electric and magnetic fields at the two boundaries (denoted A and B):

$$\begin{bmatrix} E_A \\ \\ H_A \end{bmatrix} = \begin{bmatrix} \cos k_0 h & (i \sin k_0 h)/\eta_2 \\ \\ \eta_2 i \sin k_0 h & \cos k_0 h \end{bmatrix} \begin{bmatrix} E_B \\ \\ H_B \end{bmatrix} \tag{2.16}$$

where k_0 is the wavenumber in vacuum, $h = n_2 d \cos\theta_2$ is the optical distance travelled by the wave inside medium 2, and η is called the directional optical admittance, given by

$$\eta_j = \sqrt{\frac{\epsilon_0}{\mu_0}} N_j \cos\theta_j \tag{2.17}$$

when **E** is S-polarized. When the incident light is P-polarized, the directional optical admittance is given by

$$\eta_j = \sqrt{\frac{\epsilon_0}{\mu_0}} N_j / \cos\theta_j \ . \tag{2.18}$$

Eq. 2.16 is often simply denoted by

$$\begin{bmatrix} E_A \\ \\ H_A \end{bmatrix} = \mathcal{M} \begin{bmatrix} E_B \\ \\ H_B \end{bmatrix} \tag{2.19}$$

where $\mathcal{M}$ is called the *characteristic matrix* of the layer between the boundaries at A and B. If more layers are added in a multilayer stack, the characteristic matrix of the entire system is simply the matrix product of all characteristic matrices

$$\mathcal{M} = \mathcal{M}_1 \mathcal{M}_2 \ \ldots \ \mathcal{M}_N = \begin{bmatrix} m_{11} & m_{12} \\ m_{21} & m_{22} \end{bmatrix}. \tag{2.20}$$

Hecht [40] derives general amplitude coeffiecients of reflection and transmission from a thin film based on the boundary conditions and the above relations as

$$r = \frac{\eta_1 m_{11} + \eta_1 \eta_s m_{12} - m_{21} - \eta_s m_{22}}{\eta_1 m_{11} + \eta_1 \eta_s m_{12} + m_{21} + \eta_s m_{22}} \tag{2.21}$$

$$t = \frac{2\eta_1}{\eta_1 m_{11} + \eta_1 \eta_s m_{12} - m_{21} - \eta_s m_{22}} \tag{2.22}$$

where η_s is the directional admittance of the substrate.

2.1.4 Antireflection coatings

For simplicity in the further derivation normal incidence ($\theta_1 = \theta_2 = 0°$) and non-absorptive media are assumed, meaning that the directional optical admittances η_j can be exchanged for the refractive indices n_j in Eq. 2.21. The amplitude reflection coefficient is then expressed as

$$r_1 = \frac{n_2(n_1 - n_s)\cos^2 k_0 h + i(n_1 n_s - n_2^2)^2 \sin k_0 h}{n_2(n_1 - n_s)\cos^2 k_0 h + i(n_1 n_s + n_2^2)^2 \sin k_0 h} \tag{2.23}$$

for a system with one thin film surface layer. When $k_0 h = \frac{1}{2}\pi$, Eq. 2.23 greatly simplifies, and by multiplying r_1 by its complex conjugate, an expression for the intensity reflection, or *reflectance*, can be written as

$$R_1 = \frac{(n_1 n_s - n_2^2)^2}{(n_1 n_s + n_2^2)^2} \ . \tag{2.24}$$

The reflectance is seen to equal zero when the relation between the refractive indices of the incident medium, the substrate, and the thin film is given by

$$n_2^2 = n_1 n_s \tag{2.25}$$

giving a remarkably simple expression for an antireflection coating at normal incidence.

Though not as analytically simple as Eq. 2.25, the optimal optical constants and thicknesses for antireflection coatings at non-normal incidence, for both the P and S geometry, are easily calculated using the matrix notation of Eq. 2.16. In the modelling of the optical response of a multilayered stack of magneto-optic and dielectric media described in Chapter 3, the addition of the characteristic matrices of each layer, as defined in Eq. 2.20, forms the foundation of the method to calculate the amplitude reflection components from an arbitrary number of added layers.

2.1.5 The Fabry-Perot etalon

Fig. 2.3 depicts the setup of the interferometer that was first described by Fabry and Perot in 1899 [41]. The Fabry-Perot etalon consists of two highly reflecting parallel mirrors enclosing a cavity of air or other non-absorptive media. When light is coupled into the interferometer, it can reflect back and forth between the two mirrors a number of times provided that their reflectances, $R = rr^*$, are sufficiently high. The phase delay experienced on a round trip in the interferometer is

$$\delta = \frac{2\pi}{\lambda} n_2 d \cos\theta_t \tag{2.26}$$

where λ is the wavelength of the light, θ_t is the angle of refraction, and n_2 is the index of refraction, and d is the physical thickness of the spacer layer between the mirrors [38]. The total transmittance through the Fabry-Perot is found by summing up the contributions from an infinite number of transmitted beams, and is given by

$$T_{tot} = T_1 + T_2 + \ldots T_\infty = \frac{1}{1 + F\sin^2\delta} \tag{2.27}$$

where the *finesse* of the interferometer is defined as

$$F = \frac{4R}{(1-R)^2} \tag{2.28}$$

if the reflectances of both mirrors are assumed equal. From Eq. 2.26 it can be seen that the transmittance equals unity ($R_{tot} = 0$) whenever the phase delay on one round trip is an integer multiple of π. This means that for certain thicknesses, the etalon works as a perfect anti-reflection coating. Depending on the value of the finesse parameter, the total transmittance of the Fabry-Perot can also become approximately zero, creating a perfectly reflecting mirror. The Fabry-Perot interferometer is mainly used as a tool in spectroscopy to select highly monochromatized light from a polychromatic light source. In this thesis, the interferometer effect is used to enhance the rotation experienced on reflection off a magnetic sample.

2.2 Optical rotation in magnetic media

In the absence of a magnetic field, isotropic magnetic media can be fully described by a complex dielectric constant N. However, when put in an external magnetic field, magnetic media will show optical anisotropy, meaning that the electrical permittivity in the magnetic media depends on the direction of the traversing electromagnetic

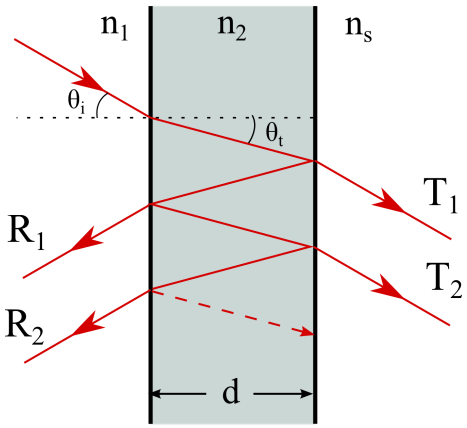

Figure 2.3: A Fabry-Perot interferometer consists of two highly reflecting mirrors used to enclose a plane parallel plate of air or another non-absorptive medium.

wave. The notion of optical anisotropy can be incorporated into the relation for the electric flux density by writing

$$\mathbf{D} = \hat{\epsilon}_{\mathbf{i,j}} \cdot \mathbf{E} \tag{2.29}$$

where $\hat{\epsilon}_{i,j}$ is the *dielectric tensor* of the medium with $i, j = 1, 2, 3$:

$$\hat{\epsilon} = \begin{pmatrix} \epsilon_{xx} & \epsilon_{xy} & \epsilon_{xz} \\ \epsilon_{yx} & \epsilon_{yy} & \epsilon_{yz} \\ \epsilon_{zx} & \epsilon_{zy} & \epsilon_{zz} \end{pmatrix}. \tag{2.30}$$

The diagonal elements ϵ_{xx}, ϵ_{yy}, and ϵ_{zz} describe the permittivity for perpendicular directions in space, whereas the off-diagonal elements are cross-terms which quantify the amount of rotation of electric fields from one spatial direction to another.

The optical rotation observed in magnetic media is a result of the polarization of the incoming light. The polarization states of an electromagnetic wave can be decomposed into two eigenmodes consisting of right circularly polarized (RCP) light, and left circularly polarized (LCP) light. Characteristic for a magnetic medium with a non-zero magnetization is that these two eigenmodes propagate with different velocities, gradually changing the state of polarization of the incident light. This magneto-optical rotation can be expressed by decomposing the permittivity tensor into a symmetric and an anti-symmetric part. By an appropriate choice of coordinate system, the diagonal elements in the permittivity tensor can be extracted for isotropic

magnetic media. The optical rotation is then visualized by the non-diagonal elements in the permittivity tensor

$$\hat{\epsilon} = \epsilon \begin{pmatrix} 1 & iQ_z & -iQ_y \\ -iQ_z & 1 & iQ_x \\ iQ_y & -iQ_x & 1 \end{pmatrix} \tag{2.31}$$

with $N = \sqrt{\epsilon}$ being the refractive index of the medium. $\mathbf{Q}$ is called the Voigt vector [42], or sometimes the *magneto-optical coupling*, related to the strength and direction of the magnetic response of the medium [4]. For a demagnetized magnetic medium $\mathbf{Q}$ is zero.

The Faraday rotation angle after an electromagnetic wave has travelled a distance L through the magnetized medium is given as

$$\Phi = -\frac{\pi L n}{\lambda} \mathbf{Q} \cdot \hat{k} \tag{2.32}$$

where λ is the wavelength, and $\hat{k}$ is the unit vector along the propagation direction of the wave. By an appropriate choice of direction of the incident wave, two components of $\mathbf{Q}$ can always be set to zero.

2.3 Surface Magneto-optic Kerr effect

The Faraday effect describes how the polarization state of light is changed when traversing through a magnetic material. However, since most magnetic materials of interest are metals that strongly absorb light, it is more convenient to experimentally measure the reflected intensity rather than the transmitted beam. As it turns out, the reflected component also exhibits magneto-optical rotation of the plane of polarization. This experimental fact was first discovered by John Kerr in 1877 [43, 44], and thereafter termed the *Magneto-optic Kerr effect* (MOKE).

2.3.1 MOKE geometries

Three different geometries are possible for MOKE experiments, namely *polar*, *longitudinal*, and *transverse* MOKE. Fig. 2.4 shows schematically how the direction of the magnetization vector within the magnetic medium with respect to the plane of incidence of the light gives rise to three different geometries for MOKE:

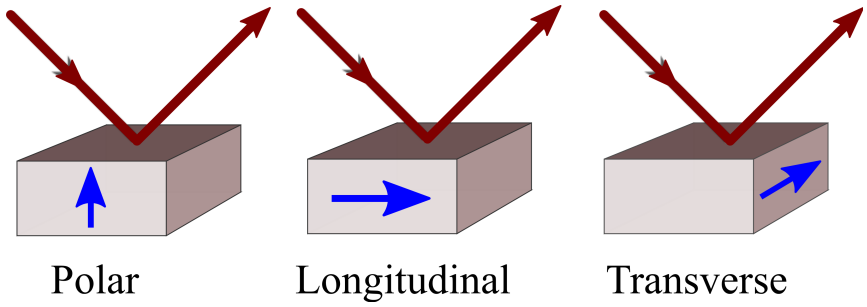

Figure 2.4: Different magnetization directions give rise to the three MOKE geometries. For *polar* MOKE, the magnetization is oriented perpendicular to the surface. In the *longitudinal* configuration, the magnetization is oriented parallel to both the surface and the incident beam. In *transverse* MOKE the magnetization is oriented parallel to the surface, but perpendicular to the incident beam.

Polar MOKE

The polar geometry, where the magnetization is oriented parallel to the plane of incidence, but perpendicular to the surface of the magnetic medium, in general gives the largest magnetic rotation. It is also the method which has been studied the most, due to its importance in magneto-optical (MO) recording technology.

Longitudinal MOKE

Longitudinal MOKE, characterized by a magnetization vector oriented parallel to both the plane of incidence and the surface of the magnetic medium, is sensitive to the in-plane magnetization on the surface of the medium. This geometry is useful when studying magnetic elements with shape anisotropy, where the physical dimension of the magnetic medium is small in one direction, e.g a magnetic ultra-thin film. In particular, longitudinal MOKE has been extensively used to study magnetic domain interactions on the micro- and nanoscale, as well as magnetic thin film structures.

Transverse MOKE

In the transverse geometry, the magnetization vector is oriented perpendicular to the plane of incidence, but parallel to the surface of the magnetic medium. Whereas polar and longitudinal MOKE both give rise to a rotation of the polarization plane of the incident light, the transverse effect only results in a modulation of the intensity.

This is due to the Kerr component of the reflected light being parallel to the normal Fresnel reflection component in the transverse geometry.

2.3.2 Definition of the MOKE signal

For MOKE the rotation angle of Eq. 2.32 is called the *Kerr angle*, Φ_k. This angle is generally complex, where the real part gives the optical rotation, and the imaginary part gives the ellipticity. This is conveniently described through the relation

$$\Phi_k = \theta_k + i\epsilon_k = \frac{k}{r} \tag{2.33}$$

where θ_k is defined as the angle between the direction of polarization of the incident light and the major axis of the polarization ellipse after reflection. ϵ_k is related to the *ellipticity* of the polarization ellipse, whereas k and r are the reflection amplitudes of the Kerr and Fresnel components of the reflectivity, respectively [4]. Fig. 2.5 shows how Eq. 2.33 is related to the polarization ellipse after reflection off a magnetic surface.

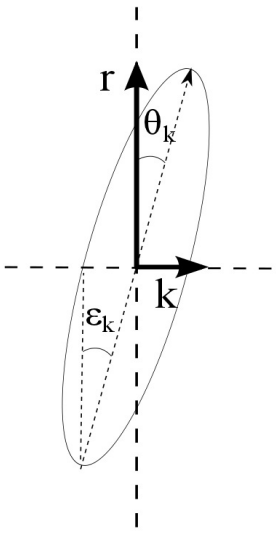

Figure 2.5: The magneto-optic Kerr effect rotates the polarization plane of light reflected off a magnetic surface. However, the rotated Kerr component k is several orders of magnitude smaller than the unrotated Fresnel component r. The angle of the polarization plane is easily recognized as the Kerr rotation $\theta_k = \tan(k/r)$, whereas the phase change generally experienced by the Kerr component on reflection also introduces an ellipticity ϵ_k.

Taking optical rotation on reflection into account, the electric fields after reflection from a thin film for S- and P-polarized light can be summarized as

$$\mathbf{E} = \begin{pmatrix} E_S^r \\ \\ E_P^r \end{pmatrix} = \begin{pmatrix} r_{ss}E_S^i + r_{ps}E_P^i \\ \\ r_{sp}E_S^i + r_{pp}E_P^i \end{pmatrix} \tag{2.34}$$

where r_{ss} and r_{pp}, following the convention used by Cantwell et al. [6], are the Fresnel amplitude reflection coefficients, whereas r_{sp} and r_{ps} are the Kerr amplitude reflection components. The first subscript represents the incident polarization, and the second the reflected polarization. In the following derivation, the subscript notation will be used instead of k and r to distinguish between the S- and P-polarized incident geometries.

2.3.3 Longitudinal MOKE signal contrast

The magnitude of the Kerr component of the reflected light is greatly exaggerated for visual purposes in Fig. 2.5. In practice, the rotated portion of the reflected light is too small to directly measure with any confidence, with the amplitude of the rotated light being typically three to four orders of magnitude smaller than the unrotated part. However, in a MOKE magnetometer setup, the rotated Kerr component is amplified and indirectly established by mixing in a small fraction of the unrotated Fresnel component before measurement, and thereafter analyzing the cross-terms. This is achieved by placing a polarization analyzer in the beam path before the photodetector. The analyzer is then rotated a small angle ϕ off the extinction angle for the Fresnel reflection, as schematically presented in Fig. 2.6.

The transmitted Kerr component is theoretically largest for $\phi = 0$. However, in this configuration, the change in measured intensity for opposite magnetization vectors will be zero, since the polarization analyzer is insensitive to the direction of the Kerr component E_{ps}. Rotating the analyzer away from extinction breaks the symmetry, and the measured intensity will be different for different directions of E_{ps}. The subsequent derivation follows the arguments presented by Allwood et al. [12], and seeks to find an analytical expression for the MOKE signal contrast without including phase differences between the components. The derivation assumes that any ellipticity in the reflected signal is eliminated by a quarter-wave before being analyzed.

The photodetectors of the experimental setup measures *intensity*, rather than amplitude, and the intensity transmitted through the analyzer for the two opposite

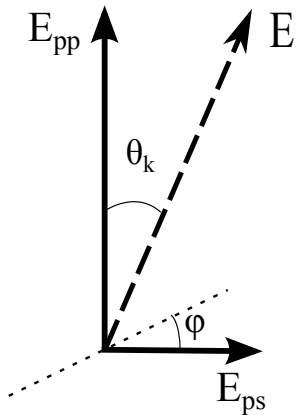

Figure 2.6: The Kerr reflection component E_{ps} (greatly exaggerated in the figure for visual purposes) rotates the polarization plane slightly off that of the incident light (here P-polarized). By inserting a polarization analyzer at an angle ϕ from extinction, a small fraction of the unrotated Fresnel component E_{pp} is mixed with a large fraction of the Kerr component.

magnetization directions can be described as

$$I_{\pm} = (E_{pp}\sin\phi \pm E_{ps}\cos\phi)^2 \tag{2.35}$$
$$I_{\pm} = E_{pp}^2\sin^2\phi \pm 2E_{ps}E_{pp}\sin\phi\cos\phi + E_{ps}^2\cos^2\phi\ . \tag{2.36}$$

If the magnetization is rapidly switching, the average signal hitting the detector is

$$I_{av} = \frac{1}{2}(I_+ + I_-) = E_{pp}^2\sin^2\phi + E_{ps}^2\cos^2\phi \tag{2.37}$$

whereas the intensity difference for opposite magnetization directions is given by

$$\Delta I = I_+ - I_- = 4E_{ps}E_{pp}\cos\phi\sin\phi\ . \tag{2.38}$$

The MOKE signal contrast for P-polarized light is then defined as

$$\frac{\Delta I}{I_{av}} = \frac{4E_{ps}E_{pp}\cos\phi\sin\phi}{E_{pp}^2\sin^2\phi + E_{ps}^2\cos^2\phi}\ . \tag{2.39}$$

A similar expression is obtained for the case of S-polarized incident light.

In the experimental setup, the incoming polarization plane is not perfectly aligned. Polarization leakage and depolarization arising from the non-planar laser light trav-

elling through the condenser and objective lenses, give a non-zero noise element which should be added to the average intensity in Eq. 2.39. The modified analytical expression for the MOKE signal contrast is then given by

$$\frac{\Delta I}{I_{av}} = \frac{4E_{ps}E_{pp}\cos\phi\sin\phi}{E_{pp}^2\sin^2\phi + E_{ps}^2\cos^2\phi + \gamma} \ . \tag{2.40}$$

γ is called the *depolarization factor*, and sums the various noise elements associated with the optical setup. If the Fresnel reflection component E_{pp} is minimized, e.g. by applying an anti-reflection coating to the magnetic thin film, γ may be the dominant factor in the denominator of Eq. 2.40, as E_{ps}^2 is inherently small, and typically one or two orders of magnitude smaller than γ.

2.4 The 4 x 4 matrix algorithm

The Matlab routine used in the modelling of the optical response of the multilayer thin film stack is based on the simplified 4 x 4 matrix algorithm as presented by Abdulhalim [10, 11]. The method calculates the 4 x 4 propagation matrix P_j for each layer $j = 1, 2, \ldots N$ in a multilayer stack. A simple matrix product then gives the total propagation matrix of the multilayer system through

$$P = P_N P_{N-1} \ldots P_j \ldots P_1 \tag{2.41}$$

analogous to the situation presented in Eq. 2.20 for a 2 x 2 matrix approach. The propagation matrix includes all the information of the optical response of the multilayer.

The combined propagation matrix is linked with the incident Ψ_i, reflected Ψ_r, and transmitted Ψ_t wavefunctions of the electromagnetic wave through matching the tangential components at the interface between the incident medium and the substrate. This relation can be written as

$$\Psi_t = P(\Psi_i + \Psi_r) \tag{2.42}$$

from which the reflection (and transmission) components of Eq. 2.34 can be extracted analytically. The amplitude reflection components are subsequently used to calculate the reflected electric field components for both S- and P-polarized incident geometry, and the MOKE signal contrast $\Delta I/I_{av}$ is calculated from Eq. 2.40. A description of the 4 x 4 matrix formulation used in the modelling part of this thesis is given in Appendix A.

Chapter 3

Modelling

3.1 Model characteristics

3.1.1 Model description

The modelling routine is based on the the expression for the longitudinal MOKE signal contrast $\Delta I/I_{av}$ in Eq. 2.40, as defined by Allwood et al. in 2003 [12], and later applied with success by others [6, 7]. The magneto-optical responses of the multilayer stacks are calculated using the 4 x 4 matrix method presented by Abdulhalim in his article from 1999 [10]. This method is here used in a Matlab© routine to calculate the reflectance coefficients from a multilayer configuration of metal, dielectric and magnetic thin films.

After calculating the reflection amplitudes of the Kerr and Fresnel components using Abdulhalim's method, Eq. 2.40 is subsequently used to predict the signal contrast, $\Delta I/I_{av}$, which is considered the figure of merit for longitudinal MOKE. The analytical expression for the signal contrast assumes that the phase difference between the Fresnel and Kerr reflection components is zero, meaning that the polarization of the reflected light (Fresnel + Kerr components) is assumed to have no ellipticity.

The depolarization factor γ is set to $6 \cdot 10^{-5}$, based on MOKE measurements on samples of silicon coated with 10 nm of permalloy. The value of γ can be interpreted as an approximate measure of the general noise floor from the optical components in the experimental setup [12], which is assumed to be approximately constant in this simple model. The validity of this assumption is further discussed in Sec. 6.4.2.

All modelling is done for linearly polarized light at an incident angle of 45° to the substrate. The incident medium is air (refractive index $n_{air} \approx 1$), and the substrate medium is Si (100). The wavelength of the incident light is set to $\lambda_0 = 635$ nm.

$\Delta I/I_{av}$ is calculated as a function of both dielectric thickness and polarization analyzer rotation angle. The model calculates the multilayer system response to both P- and S-polarized incident light. In the following discussion only the modelling results for P-polarized light will be presented. The modelled curves for S-polarized incident light can be found in Appendix B, and will be addressed whenever they predict results which are different from the P-polarized case.

3.1.2 Refractive indices

Several different multilayer combinations of materials have been produced in the experimental part of this project, in trilayered or quadrilayered stacks of thin films on silicon substrates. The refractive indices of these materials are generally well known, and is presented in Table 3.1. The off-diagonal permittivity elements of the magnetic materials, responsible for the magnetic rotation, are not as well represented in literature, and the values reported often vary from source to source. The off-diagonal permittivity element of permalloy (Py) also varies for different compositions of the alloy. The value used in the modelling was estimated from the best model fit to the measured signal contrast from a bare 10 nm thin film of Py on Si. Uncertainties related to the off-diagonal permittivity are discussed in Appendix D.3.

Table 3.1: Refractive indices and off-diagonal dielectric permittivities of the materials used in this project. All values are taken from Handbook of Optical Constants of Solids [48] for a wavelength of 630-640 nm, except where mentioned otherwise.

Material	Formula	Refractive index	Off-diagonal permittivity
Gold	Au	0.17 + 3.15i[a]	-
Aluminium	Al	1.51+ 7.65i	-
Silicon	Si	3.87 + 0.018i	-
Zinc sulfide	ZnS	2.35	-
Magnesium fluoride	MgF_2	1.38	-
Nickel	Ni	1.99 + 4.02i [45]	(0.1 $\rightarrow$ 0.25) - 0.04i[b] [46]
Permalloy	$Ni_{84}Fe_{16}$	2.4 + 3.7i [47]	0.3 - 0.06i[c]

a) For a wavelength of 650 nm.

b) The value varies for different source experiments.

c) Fitted value

3.2 Dielectric overlayer configuration

As already shown both theoretically and experimentally by Cantwell et al. [6], the reflected Kerr signal contrast is enhanced by a factor of 2-2.5 when a thin film of the magnetic material Ni is overcoated with the dielectric ZrO_2. This overlayer enhancement is confirmed by the theoretical model also for other magnetic and dielectric materials.

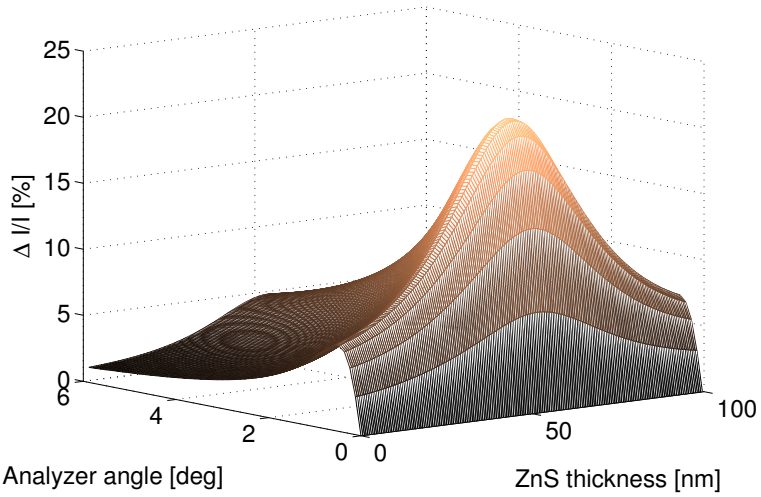

Figure 3.1: Modelled longitudinal Kerr signal contrast $\Delta I/I_{av}$ for P-polarized incident light as a function of analyzer angle and ZnS overcoat thickness. The magneto-optical layer is a 10 nm thick layer of Py, coated on top of a 100 nm thick layer of Al on a Si substrate. Maximum enhancement is predicted for a ZnS thickness of 53 nm.

Fig. 3.1 shows the predicted Kerr signal contrast as a function of the thickness of the ZnS overcoating and the angle of the analyzer for a 10 nm thin film of permalloy on a silicon substrate coated with 100 nm aluminium. Both S- and P-polarized incident light experience an enhancement in the Kerr signal contrast at a ZnS thickness of about 53 nm.

It is possible to model the maximum signal contrast for a 10 nm thick permalloy layer coated with dielectrics with variable refractive indices. Fig. 3.2 shows the modelled maximum $\Delta I/I_{av}$ as a function of the refractive index of the overcoated dielectric. Maximum enhancement is predicted for materials with high refractive indices both for S- and P-polarized light. For a permalloy thin film of greater thickness than 10 nm (not shown here), maximum enhancement is predicted for a refractive

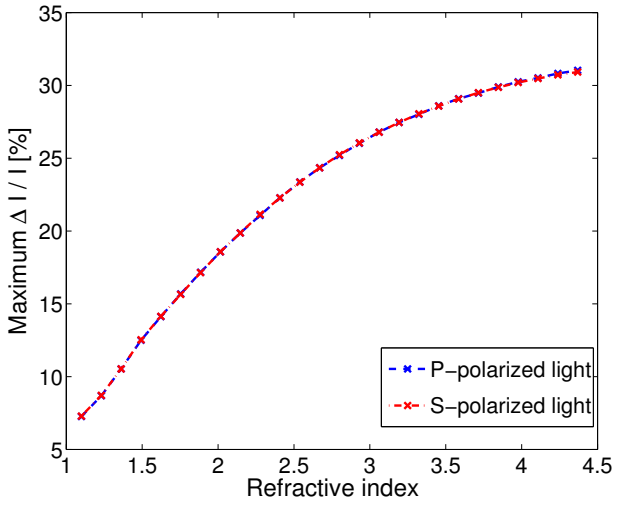

Figure 3.2: The modelled maximum MOKE signal contrast $\Delta I/I_{av}$ as a function of the refractive index of the dielectric coating. The signal contrast is seen to be largest for coatings with refractive indices higher than that normally observed among dielectrics.

index of approximately 4. Dielectrics with a refractive index this high which are also transparent to visible light, are not found in nature, though ZnS (refractive index $n_{ZnS} = 2.35$) is a high-index dielectric suitable for this purpose.

An intriguing possibility would be to do MOKE measurements in the infra-red, where Si can be used as the anti-reflection coating 'dielectric'. Whereas silicon is strongly absorbing and opaque in the visible regime, it is transparent in the infra-red [37]. However, further investigations into the use of infra-red light in MOKE studies are beyond the scope of this thesis.

3.3 Dielectric underlayer configuration

The possibility of enhancing the Kerr signal by applying a dielectric layer *below* the magneto-optic layer might at first seem counter-intuitive, since the optical rotation happens above the dielectric. However, by adding a reflecting metal layer on top of the substrate, below the dielectric, the incoming light might be rotated on reflection multiple times: A dielectric underlayer enclosed by two reflecting metal thin films creates a Fabry-Perot etalon below the magnetic layer. For certain dielectric thicknesses, which can be estimated from Eq. 2.27, interference effects amplify or reduce one or both of the reflected Fresnel and Kerr components.

Fig. 3.3 shows how the enhancement of the MOKE signal contrast is centered around a resonance peak at a MgF_2 thickness of approximately 210 nm. Furthermore, the MOKE signal contrast almost vanishes at a MgF_2 thickness of approximately 250 nm. These are two distinct features in the $\Delta I/I_{av}$ curve which should be possible to experimentally observe if the correct MgF_2 thicknesses are produced below the permalloy thin film.

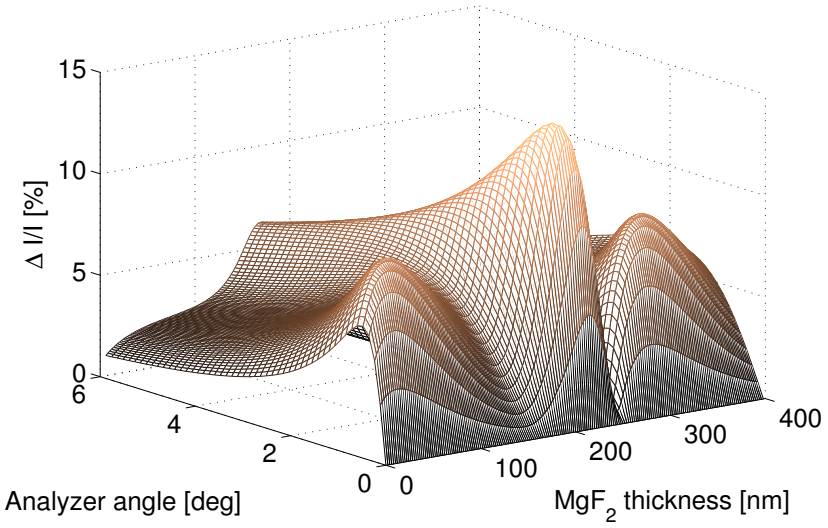

Figure 3.3: Modelled longitudinal Kerr contrast $\Delta I/I_{av}$ for P-polarized incident light as a function of analyzer angle and MgF_2 thickness. The magneto-optical layer is a 10 nm thin film of Py, which is coated on top of a variable thickness MgF_2 layer. The substrate is Si, coated with a 100 nm thick reflecting layer of Al. Maximum enhancement is predicted for a MgF_2 thickness of 210 nm.

The maximum MOKE contrast achieved by applying a dielectric coating *below* the magnetic layer can also be modelled as a function of the dielectric refractive index. The results are shown in Fig. 3.4, predicting stronger enhancement for low-index dielectrics. This is in sharp contrast to the case of an overcoating, where a high-index dielectric gives the largest contrast enhancement.

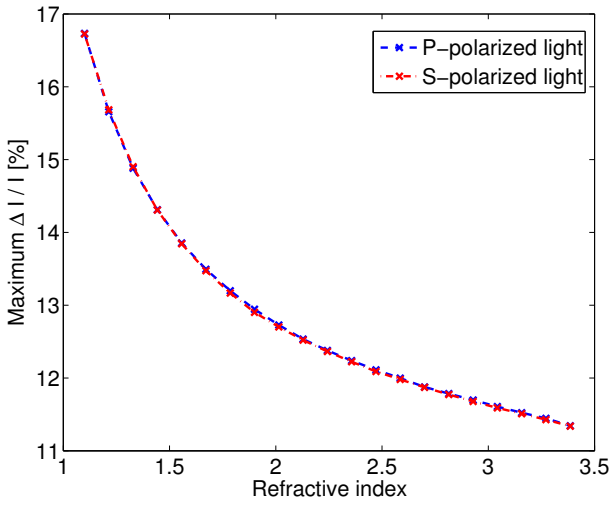

Figure 3.4: The maximum MOKE signal contrast $\Delta I/I_{av}$ modelled as a function of the refractive index of the dielectric underlayer. No definite peak is seen in the enhancement factor, though low-index dielectrics give stronger enhancement.

3.4 Quadrilayer configuration

The previous sections show how both a high-index dielectric overlayer and a low-index dielectric underlayer enhances the longitudinal MOKE signal contrast from a magnetic thin film, provided the substrate is close to totally reflecting. The possibility of combining these two effects, by sandwiching a thin magneto-optic layer between high-index and low-index dielectrics in a quadrilayer configuration, seems inviting.

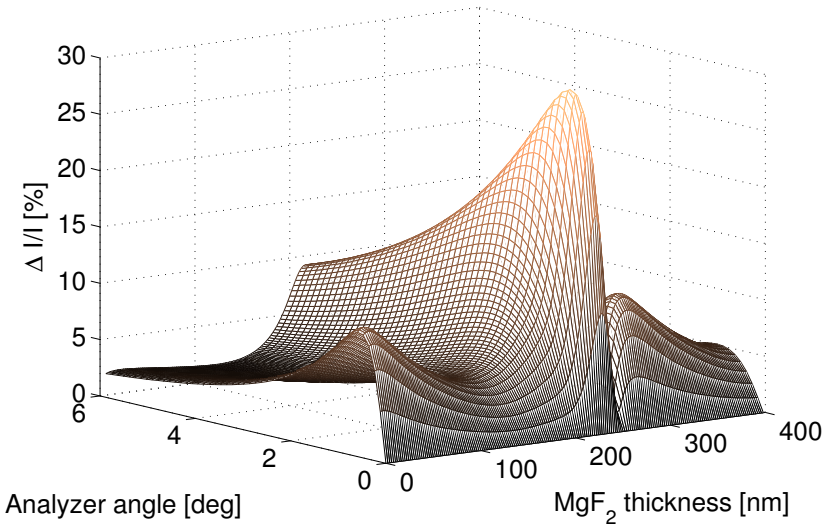

Figure 3.5: Modelled longitudinal Kerr contrast for P-polarized incident light as a function of analyzer angle and MgF_2 thickness. The magnetic layer is a 10 nm thin film of Py. A dielectric underlayer of variable thickness MgF_2 is applied, as well as a 80 nm overcoating of ZnS. The substrate is Si, coated with a 100 nm reflecting layer of Al. Maximum enhancement is observed for a MgF_2 thickness of 230 nm.

Fig. 3.5 confirms that the enchancement of the MOKE signal contrast is predicted to be substantial for a quadrilayered configuration where the magnetic Py thin film is deposited on top of the low-index dielectric MgF_2, and subsequently overcoated with a 80 nm thin film of the high-index dielectric ZnS. The maximum $\Delta I/I_{av}$ in this configuration is predicted to be as high as 30%, which is an enhancement of a factor 4.9 compared to the bare Py thin film on Si.

The curve for P-polarized light looks the most promising for the quadrilayered configuration (S-polarized curves are presented in Appendix B), since the large

$\Delta I/I_{av}$ here is due to both a large rotated Kerr component and a substantially large unrotated Fresnel component, giving a higher total intensity hitting the detector. Fig. 3.6 shows the predicted intensity reflectance of the Fresnel and Kerr components for both P- and S-polarized light. It can be seen that the Fresnel reflectance approaches zero for S-polarized light at the MgF_2 thickness where the Kerr component is highest. This situation is believed to give larger uncertainties due to low measured intensity values.

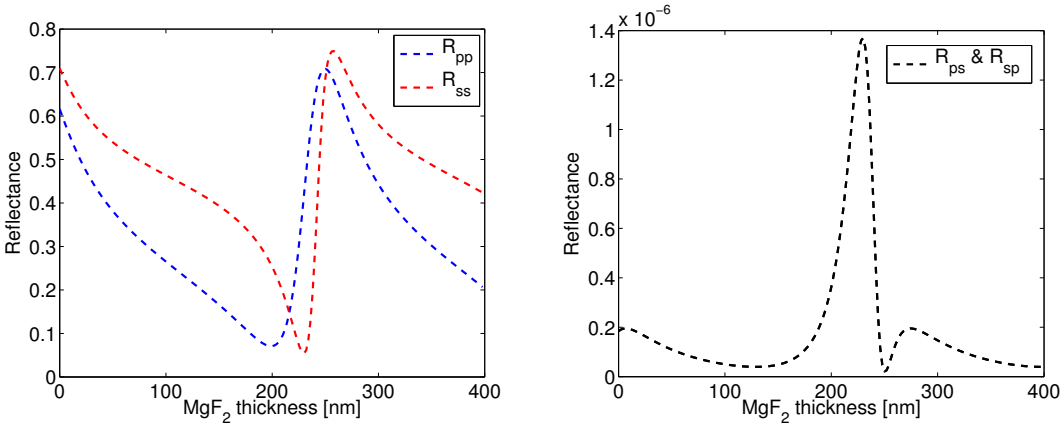

Figure 3.6: The modelled Fresnel (**left**) and Kerr (**right**) reflectance / intensity reflection as a function of MgF_2 thickness for the quadrilayered structure of 100 nm Al, MgF_2, 10 nm Py, and 80 nm ZnS on a Si substrate. For S-polarized light the lowest reflectance is predicted where the total Kerr rotation is largest.

Chapter 4

Experimental

4.1 Sample preparation

Silicon (100) wafers, approximately 2 x 2 cm in size, were cleaned with acetone, $(CH_3)_2CO$, and isopropanol, $(CH_3)_2CHOH$, and placed in a supersonic bath for five minutes to remove any contaminations on the surface. The samples were subsequently rinsed with deionized water with a resistivity larger than 18 MΩm, and blown dry using compressed N_2 gas. After inspection, the samples were placed in a vacuum chamber for deposition. Parts of the samples were masked to create clean edges for thin film thickness measurements.

4.1.1 Physical vapour deposition

The thin film multilayer structures were produced in a CMK III vacuum deposition system. A diffusion pump cooled with liquid N_2 pumped the vacuum chamber to a pressure below 6×10^{-6} Torr in a pumpdown time of 2.5-3 hours. The method of deposition is called resistive evaporation [49], and is characterized by heating a conducting basket or boat by driving an electric current through it. The material to be evaporated is placed in the basket / boat, and starts evaporating after being heated above the sublimation temperature in an evacuated atmosphere.

The thickness of the evaporated thin films were monitored using two Inficon XTM[4] crystal thickness sensors placed in the vicinity of the substrates inside the vacuum chamber. The deposition rate for heavy metals (Ni, Au, $Ni_{84}Fe_{16}$) was 4-7 Å/s, for MgF_2 15-25 Å/s, for Al 10-12 Å/s, and for ZnS 7-8 Å/s.

[4] www.inficonthinfilmdeposition.com

Graded interfaces

To be able to measure the MOKE signal contrast for different thicknesses of the dielectric under- and overlayer, a method was implemented to make dielectric thin films with varying thickness in one direction along the surface of the sample. The MOKE measurements are performed with a focused laser beam (see Sec. 4.2), opening up the possibility to select different locations on the sample. The graded interfaces thus make it possible to compare MOKE signals for varying dielectric thicknesses.

The graded interfaces were produced by placing an aluminium barrier between the evaporation source and the substrate during deposition, partially covering the surface of the substrate. The barrier is placed approximately 5 cm below the substrate, blocking parts of the stream of particles from the evaporation source. This simple technique results in a dielectric thickness gradient on the surface of the substrate over an area which is 6-8 mm wide.

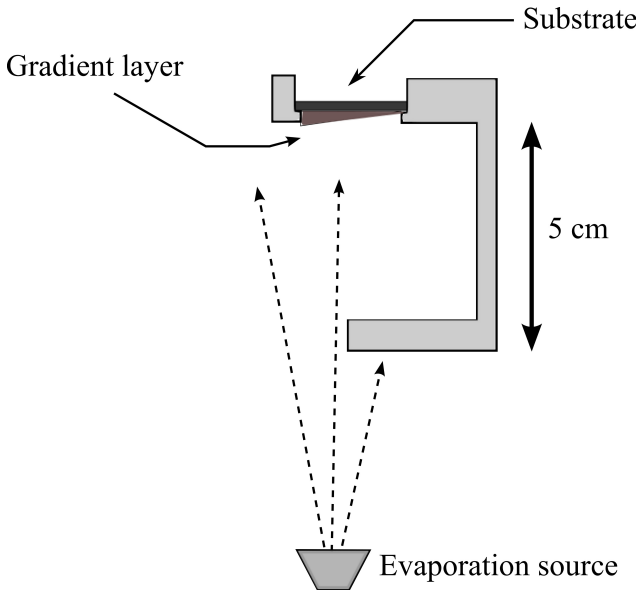

Figure 4.1: Schematic image of how the graded interfaces are produced by blocking parts of the particle beam from the evaporation source (MgF_2 or ZnS) by an aluminium barrier placed approximately 5 cm below the substrate holder.

4.1.2 Thickness determination

The thicknesses of the thin films after deposition were verified for selected samples using a Tencor Alpha-Step®100[5] profilometer. For gradient thickness layers a part of the substrate was masked perpendicular to the gradient direction, and the thickness was determined as a function of the lateral distance on the wafer.

The thickness of the thin film of permalloy was also measured using *atomic force microscopy* (AFM) due to its small thickness challenging the resolution limits of the Tencor profilometer. The AFM used was a Veeco (di) MultiMode V[6] from Dymek Company Ltd.

4.1.3 Multilayer structure

Fig. 4.2 shows a schematic layout of the different layers in the quadrilayer configuration. The Al serves as a close to totally reflecting layer used as a basis for the rest of the multilayer structure, preventing light from being transmitted and absorbed in the Si substrate. The dielectric layers of MgF_2 and ZnS are graded, where the thickness gradient of the ZnS is oriented perpendicular to the thickness gradient of MgF_2, so a wide range of dielectric thickness combinations can be measured on the sample surface.

Fig. 4.2 shows the configuration of the quadrilayered sample used for the final MOKE signal contrast measurements. Preliminary samples with other configurations were also made, using Ni instead of Py, and Au (where Cr is used as an adhesive to the Si substrate) instead of Al.

[5] An older analog version of the Tencor Alpha-Step®D-100, http://www.kla-tencor.com/surface-profiling/alpha-step-d-100.html

[6] http://www.dymek.com/Dymek-products-5-006.aspx

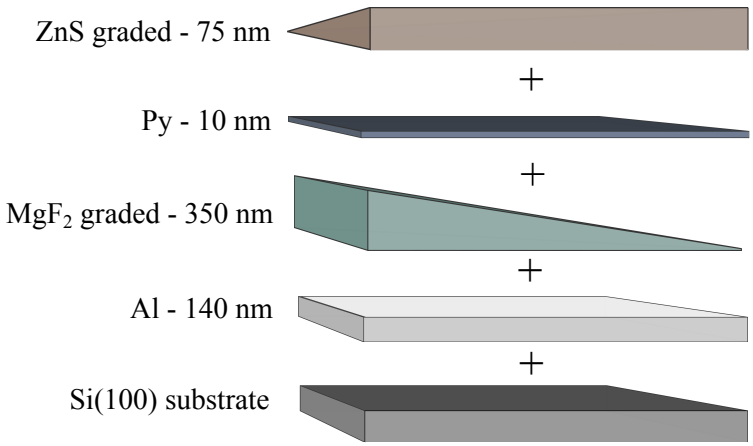

Figure 4.2: Schematic figure of one of the quadrilayer thin film stacks produced by vacuum evaporation. The ZnS thickness gradient is oriented perpendicular to the MgF_2 gradient. When depositing the dielectric layers, regions of the samples were masked to enable measurements of the Kerr signal contrast from bare Py on Si and Si + Al. For visual purposes, the layer thicknesses are not to scale.

4.2 NanoMOKE

The NanoMOKE^{TM}2 experimental table is constructed by Durham Magneto Optics Ltd. as an integrated system to measure the longitudinal and/or transverse magneto-optic Kerr effect by the help of a semiconductor laser, two electromagnets, a polarizing beam splitter, a quarter-wave ($\lambda/4$) plate, a polarization analyzer, and focusing optics. The system can be set up to measure either the longitudinal or the transverse Kerr effect, and both P- and S-polarized incident laser light can be utilized. The optics are mounted on an optical table, and connected to a control rack with a computer and power supplies for the electromagnets.

4.2.1 Experimental setup

Fig. 4.3 shows a schematic image of the experimental setup for the MOKE magnetometer used for longitudinal MOKE measurements in this project. The setup is mounted on an optical table where the electromagnets and sample motion stage are controlled by a computer.

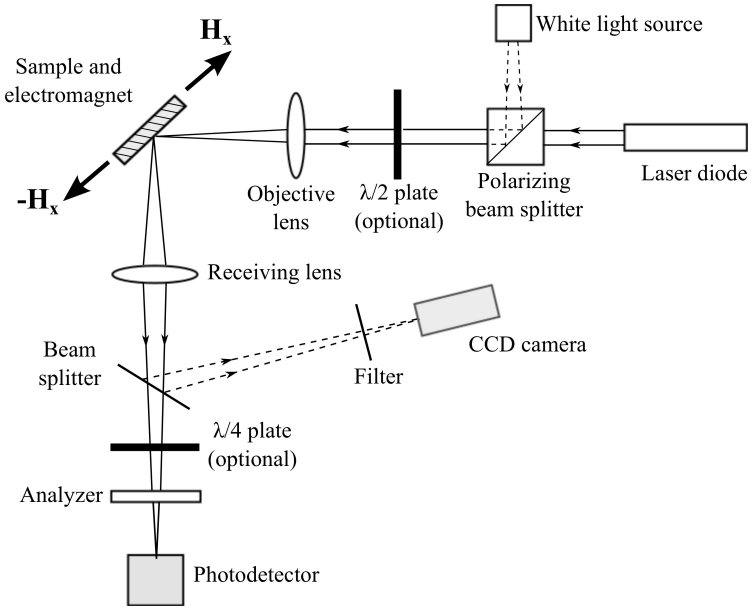

Figure 4.3: A schematic drawing of the components in the NanoMOKE 2 magnetometer setup. White light is mixed into the beam path to image the sample surface. The light is P-polarized by default, though S-polarized light can be chosen by inserting a half-wave ($\lambda/2$) plate at 45° before the objective lens. The quarter-wave ($\lambda/4$) plate is inserted to measure Kerr ellipticity instead of Kerr rotation.

Laser and optics

The laser light comes from a 4.5 mW current and temperature stabilized laser diode with a wavelength of 635 nm (630 - 640 nm). The laser class is 3R (IEC 60825-1). The laser light is first sent through a polarizing beam splitter cube where the polarization is set to the horizontal plane. For a vertically aligned sample, this polarization is in the plane of incidence, and hence the incident light is P-polarized by default. A half-wave plate rotated at 45° can be inserted after the polarizing beam splitter to switch the incident light to S-polarized.

At the beam splitter cube white light is mixed into the beam path for illumination of the sample for imaging the sample surface using a microscope CCD camera. The beam is further focused down on the sample by the objective lens, giving a laser beam spot of approximately 5 μm in diameter at optimal focusing. The receiving lens collects the light and focuses the laser onto the photodetector.

Motion stage and sample imaging

The sample is mounted on an X-, Y-, Theta- motion stage for vertical, horizontal, and rotational movement of the sample, The motion stage can be controlled with micrometer precision, allowing good control of the laser beam position on the sample. After reflecting off the sample at an angle of 45°, the laser beam goes through a beam splitter. The reflected light from the beam splitter continues through a filter to the CCD camera for imaging of the sample surface.

The image from the CCD camera shows an approximate 400 x 400 μm selection of the sample surface. The image is used to select interesting features on the sample surface, as well as being a helpful tool when focusing the laser beam spot. Since the angle of incidence is 45°, the image is sharply focused only along a vertical stripe down the middle. The oblique angle of incidence also causes the laser beam spot to have a non-gaussian profile. The focusing is done by eye, minimizing the amount of higher order harmonics in the beam profile. Fig. 4.4 shows an image of the laser spot on the surface of a MgF_2 coated sample, in the vicinity of the coating edge.

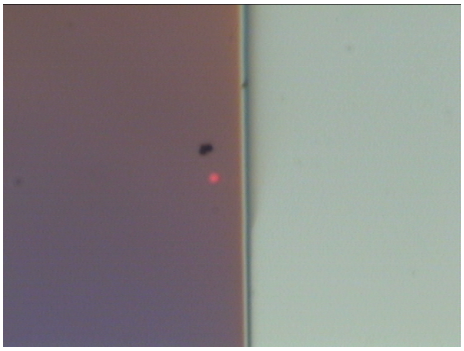

Figure 4.4: After attenuation the laser spot can be imaged on the substrate surface by a CCD camera, here in the vicinity of a MgF_2 coating edge and a micrometer sized dust particle on the surface. The image width is 400 μm, and the focused laser spot has a full width at half maximum of approximately 5 μm. Due to the 45° incidence angle, the surface is in focus only along a vertical stripe down the middle of the image.

Analyzer and quarter-wave plate

The intensity of the rotated Kerr component of the reflected light is typically five to seven orders of magnitude less intense than the unrotated Fresnel component. This fact makes direct measurement of the Kerr component inherently difficult. To

circumvent this problem a small portion of the unrotated Fresnel component of the incoming light is mixed with a large portion of the rotated Kerr signal to be able to experimentally observe the optical rotation through cross-terms in the intensity while rapidly switching magnetization directions. Practically this is accomplished by placing a polarization analyzer in the laser beam path after reflection, and subsequently rotating this analyzer slightly off the extinction angle to let some of the unrotated light come through.

If the rotated Kerr reflection component is phase delayed with respect to the Fresnel reflection, the resulting light will be elliptically polarized. A quarter-wave ($\lambda/4$) plate can be inserted into the beam path before the polarization analyzer to switch the signal from Kerr rotation θ_k to Kerr ellipticity ϵ_k. The quarter-wave plate is not strictly necessary to measure the Kerr effect, though it is believed that it can be used as a means to remove the ellipticity of the Kerr signal altogether, as described in Sec. 4.2.2.

Photodetectors

The NanoMOKE$^{\text{TM}}$2 system is equipped with two photodiodes which measure the intensity of the light reflected off the surface of a substrate. The photodiodes saturate when the beam intensity gives a signal higher than 5000 mV, making MOKE signal contrast measurements for angles larger than approximately 6° off the minimum value impossible without introducing filters. However, since the maximum signal contrast is usually observed somewhere between 0.5° and 2° rotation of the polarization analyzer, this is not considered to be an experimental drawback.

4.2.2 Experimental procedure

The software controlling the experimental table is called LX Pro, and is developed by Durham Magneto Optics Ltd. From LX Pro's *Dashboard*, the motion of the sample holder can be controlled. Furthermore, LX Pro controls the power supplies for the electromagnets, which can be programmed to run alternating current loops through the electromagnets. The magnetic field strength, and the frequency of the current loops, are set through LX Pro. In this project, magnetic field strengths of 150 Oe are typically applied (The unit **Oersted**, for magnetic field strength, is defined as $1000/4\pi$ amperes per meter in SI units.).

Since the figure of merit in this thesis is the Kerr signal contrast $\Delta I/I_{av}$, and not the Kerr rotation angle θ_k directly, the experimental procedure requires the measurement of the reflected intensity in both magnetization directions. This is accomplished by placing the sample in between two electromagnets, where the magnetic field can

be changed rapidly (at 27 Hz) by an external power supply. The resulting hysteresis loop gives both the MOKE signal and the average intensity.

A method to remove the ellipticity of the Kerr signal with the help of the quarter-wave plate is usually implemented in the experimental procedure at every new position of measurement: By iteratively minimizing the intensity at the photodetectors by rotating the angle of the quarter-wave plate and the angle of the polarization analyzer, any ellipticity in the reflected light is believed to be eliminated [13]. The maximum Kerr signal is observed where there is no phase mismatch between the Kerr component and the Fresnel component. This condition of no phase mismatch is also an assumption in the derivation of $\Delta I/I_{av}$. However, the iterative intensity nulling procedure was later found not to give the desired results for complex multilayered samples. A full discussion of the impact of the quarter-wave plate in the experimental setup is presented in Sec. 6.3.

4.2.3 Hysteresis loops

A typical hysteresis curve for a 10 nm thin film of permalloy deposited on top of a MgF_2 coating is depicted in Fig. 4.5. The hysteresis loop results from a sinusoidal magnetic field switching cycle of approximately 150 Oe. The figure shows how the photodetector intensity, given in mV, varies as a function of the magnetic field strength. The intensity transmitted through the polarization analyzer depends on the strength and direction of the magnetization vector in the magnetic thin film. The MOKE signal contrast $\Delta I/I_{av}$ is easily calculated from the hysteresis curve as the ratio of the difference in intensity to the average intensity. Hysteresis loops are typically averaged over 200 - 1000 cycles, and takes from 10 to 60 seconds to measure. A higher number of averaging cycles results in a better defined signal.

For each position on the sample, hysteresis loops are measured for different rotation angles of the polarization analyzer, usually up to 6°. Following the definition of $\Delta I/I_{av}$ in Eq. 2.40, zero Kerr signal ΔI defines the zero point of the analyser angle ϕ. When the nulling procedure of the quarter-wave plate and analyzer is followed, this angle also gives the lowest photodetector intensity. The quarter-wave plate rotation angle must in general be optimized at each new position on the sample surface due to different reflection and phase conditions.

The data files from each hysteresis loop are ordinary text files, which can easily be read by e.g. Matlab. MOKE signal contrast curves are plotted as 3D graphs, as a function of both the position on the sample and the analyzer angle. Sample positions are then subsequently transferred to dielectric thicknesses after measuring the thickness gradient on the sample surface.

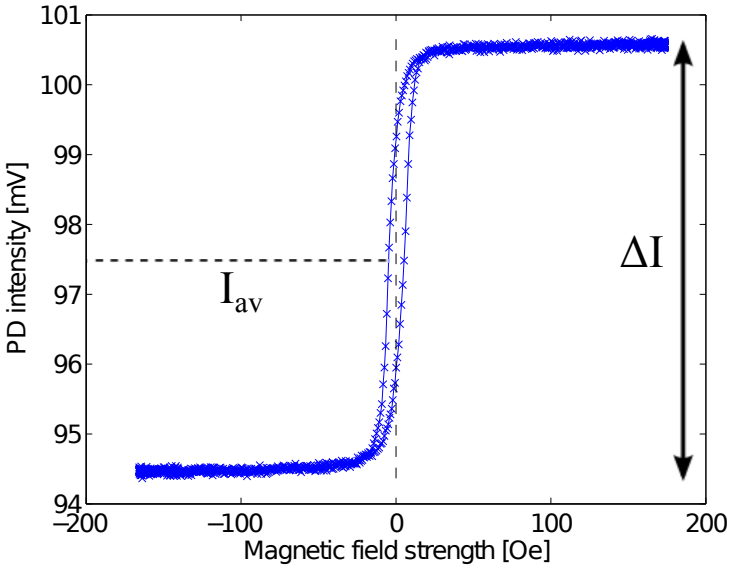

Figure 4.5: A typical hysteresis loop from a sample with a magnetic thin film of permalloy. The intensity is read in mV by the photodetector, whereas the strength of the magnetic field is given in Oersted [Oe]. The loop is averaged over 300 magnetic field cycles.

The magnetic thin films studied in this project are mostly made of permalloy ($Ni_{84}Fe_{16}$), though some samples were also made using nickel. Permalloy is generally preferred when making magnetic devices and nanostructures because of its high magnetic permeability and low coercivity [50]. The low coercivity of permalloy can be recognized in Fig. 4.5 from the small width of the hysteresis curve. Thus only a small coercive field is needed to flip the magnetization direction within the thin film.

4.2.4 Analyzer angle readout

The polarization analyzer situated before the photodetector in the beam path is held in an HPR 221 standard polarizer rotator from CVI Melles Griot[7]. Even though the analyzer holder is sensitive enough for the small angle adjustments required in a longitudinal MOKE experiment, the manual angle readout accuracy is not better than $\pm 0.2°$. This low readout resolution is circumvented by the fact that the measured intensity on the photodetector scales with the analyzer angle. Thus the rotation of

[7]https://www.cvimellesgriot.com/Products/products.aspx

the analyzer for small angles is derived from the theoretical asymptotic form of the average intensity

$$I_{av} = a \sin^2 \phi + b \tag{4.1}$$

where b is the minimum intensity defining $\phi = 0°$, and a is a proportionality factor calculated from the intensity at a known angle, e.g. $4°$, as used in this experiment. Though the calculated intensities are still affected by uncertainties from the estimation of a and b, the precision of this method of determining small angles is believed to greatly exceed that of manual readout. Error estimates related to intensity readout and analyzer angle determination are further discussed in Appendix D.1.

Chapter 5

Results

5.1 Sample overview

Several samples were made using both nickel and permalloy magnetic thin films to test the modelled results showing longitudinal MOKE signal contrast enhancement for dielectric coatings. Table 5.1 lists the different samples and their multilayer structures. Both Al and Au (with a thin underlayer of a Cr adhesive) were used as a reflecting base layer. However, Al was usually preferred due to high deposition currents causing heating in the electrical cables when doing resistive evaporation of Au.

The experimental focus was mainly on the trilayered (dielectric underlayer) configuration, since the overlayer enhancement effect has already been shown by others [7, 6]. However, positive results from trilayer samples with a MgF_2 underlayer also encouraged the fabrication of two quadrilayer samples with a sandwiched Py thin film configuration. It should be noted that samples 1-3 provided preliminary results of a proof of concept. After positive preliminary results, 10 nm Py was chosen as the most interesting magnetic thin film for further studies, due to the interest in ultra-thin films in domain wall motion research [3, 8].

Sample 6 was made to test whether the quadrilayer results for 10 nm Py thin films were reproducible using Au as a reflecting layer. Only sample 4 (trilayer) and 5 (quadrilayer) are discussed in detail in this chapter, though additional results are presented in Appendix C.

Table 5.1: List of samples made with CMK III deposition system for longitudinal MOKE measurements. All samples were made from cleaned Si (100) wafers.

#	Metal	Dielectric under-/overlayer	Magnetic
Preliminary samples			
1	Cr (5 nm) + Au (100 nm)	MgF_2 (0-350 nm)	Ni (20 nm)
2	Al (100 nm)	MgF_2 (0-350 nm)	Py (20 nm)
3	Al (100 nm)	MgF_2 (0-400 nm)	Ni (10 nm)
Main samples			
4	Al (140 nm)	MgF_2 (0-400 nm)	Py (10 nm)
5	Al (140 nm)	MgF_2 (0-400 nm) / ZnS (0-75 nm)	Py (10 nm)
Reproducibility test sample			
6	Cr (2 nm) + Au (78 nm)	MgF_2 (0-400 nm) / ZnS (0-75 nm)	Py (10 nm)

5.1.1 Enhancement factor

The longitudinal MOKE *enhancement factor* is defined as the ratio of the Kerr signal contrast $\Delta I/I_{av}$ on dielectric coated areas of a sample to that of the bare magnetic thin film on silicon. Table 5.2 presents the enhancement factors for the different samples studied in this project. The results are given for P-polarized incident light, since this is the default polarization of the experimental setup, and only the main samples were also measured with S-polarized incident light.

It can be seen that permalloy generally gives a higher Kerr signal contrast than nickel. However, the maximum enhancements observed for the two different magnetic materials are comparable. Both signal contrast and enhancement factors are seen to be lower for thinner films. This is in some ways expected, since thinner magnetic structures give smaller Kerr components. A small Kerr signal is more affected by general noise, especially at small analyzer angles, where the enhancement is predicted to be highest.

The discrepancy between the bare Py results for trilayer sample 4 and quadrilayer sample 5 might be attributed to slight differences in magnetic permalloy thickness for the two samples, or that the permalloy in the case of the trilayered sample, being exposed to air for longer periods, reacts with the air to form a thin layer of oxide on the surface.

Table 5.2: Enhancement factors for measured samples.

#	$(\Delta I/I_{av})_{Si}$ [%]	$(\Delta I/I_{av})_{max}$ [%]	Enhancement
1	4.45	9.86	**2.22**
2	8.16	17.50	**2.14**
3	3.06	5.35	**1.75**
4	6.53	11.52	**1.76**
5	5.72	23.17	**4.05**
6	5.93	23.40	**3.95**

The following sections present the most important results obtained from the NanoMOKE^{TM}2 system for the trilayer sample 4, with a MgF_2 underlayer, and the quadrilayer sample 5, with both a MgF_2 underlayer and a ZnS overlayer. The longitudinal MOKE signal contrast $\Delta I/I_{av}$ was calculated as a function of the angle of the polarization analyzer, and further as a function of the position on the wafer surface. The dielectric thickness at each position was then subsequently determined by matching the lateral position to the measured thickness profile.

The results presented are for P-polarized incident light. Parallel experiments were made for S-polarized light, presented in Appendix C.2. The results for the two different polarization geometries are to a large extent similar, though they deviate at some important multilayer configurations. These deviations, and their impact on the theoretical model, will be further discussed in Chapter 6.

5.2 Thickness determination

5.2.1 Profilometer measurements

The thickness of the dielectric under- / overlayer varies over the surface of the wafer as described in Sec. 4.1.1. Hence, a Tencor Alpha-Step®100 profilometer was aplied to verify the thicknesses of the dielectric films.

The results from the thickness measurements on the quadrilayer sample 5 are presented in Fig. 5.1. As can be seen from the figure the MgF_2 thickness increases almost linearly in a 5-6 mm region in the middle of the sample, and rounds off to a final thickness of approximately 400 nm. The MgF_2 gradient measured on the trilayered sample 4 closely resembles the one for sample 5.

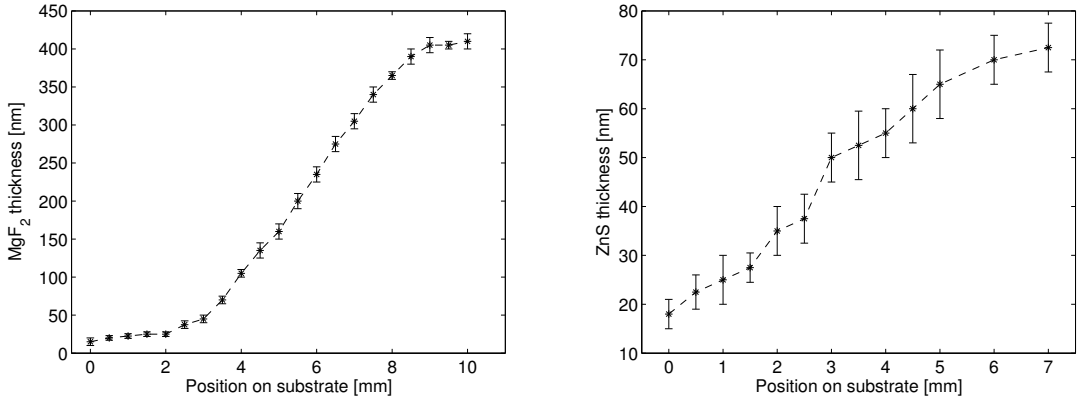

Figure 5.1: The thickness gradients of MgF_2 (**left**) and ZnS (**right**) for the quadrilayer sample 5 measured by the AlphaStep profilometer.

The ZnS gradient is more difficult to determine, and has larger uncertainties, due to its smaller thickness approaching the resolution limit of the profilometer. The start and end points of the gradient were not accessible for measurement, though the thickness is seen to increase close to linearly for a region of 5-6 mm on the substrate surface, reaching a final thickness of about 75 nm.

The error bars represent the uncertainty in the manual readout, which is estimated from the fluctuations in thickness observed at a presumably flat surface. An example of a profilometer graph paper is presented in Appendix D.2. The position on the sample was changed by turning a manual knob with length scalebar. From this scalebar the uncertainty in positioning on the wafer surface was estimated to be approximately ± 0.05 mm

5.2.2 AFM measurements

The thickness of the permalloy thin film for the trilayered sample 4 was measured at two places using AFM. Fig. 5.2 shows an AFM micrograph of the Py thin film edge and the height profile measured. Both AFM measurements suggest a Py thickness of approximately 10 nm, which will also be assumed for the quadrilayered sample 5 in the following discussion.

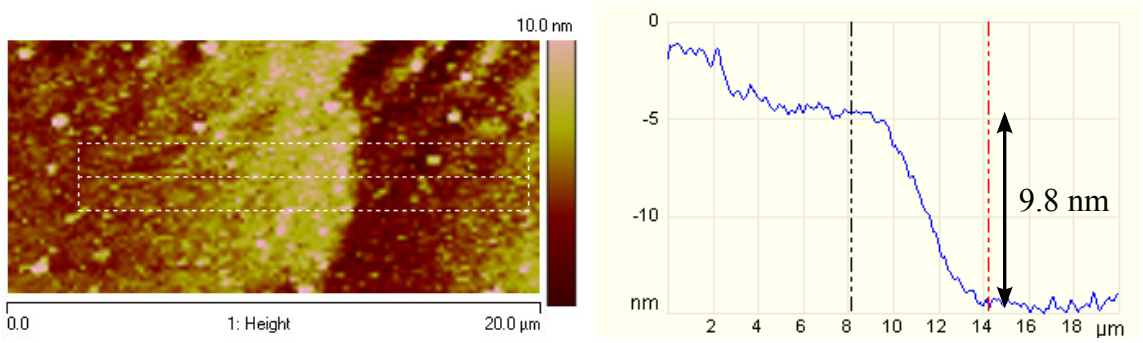

Figure 5.2: AFM surface scan image **(left)** and height profile **(right)** for the 10 nm permalloy thin film edge of sample 4. The images were generated using the software of the Veeco (di) MultiMode V instrument. The height profile is corrected for the slope seen in the AFM image. Note that the height profile is averaged over the whole image, not only in the highlighted region.

5.3 Simple Py thin films

Parts of the samples were masked when depositing the graded MgF_2 coating, so the magnetic rotation of a thin film of bare permalloy could be measured. Fig. 5.3 shows the signal contrast from a silicon (100) wafer coated with only a 10 nm thin film of permalloy $Ni_{84}Fe_{16}$. The result from this experiment was used to fine-tune the value of the depolarization factor γ. The model shows reasonable agreement with the experimental data when the value of γ is set to $6 \cdot 10^{-5}$. The off-diagonal permittivity element of permalloy is fitted to $\epsilon_{xy} = 0.3 - 0.06\mathrm{i}$, which is slightly higher than the value reported by Berger et al [47].

The maximum signal contrast for a 10 nm thin film of permalloy on silicon was found to be 6.53%. For Py on the reflecting layer of 140 nm Al, the maximum signal contrast drops to 4.77%, in contradiction to the model predictions that the signal contrast is larger for an aluminium underlayer. The model gives a better fit to the experimental data for Py on Al when the value of γ is raised to $1.1 \cdot 10^{-4}$, showing that the assumption of a constant depolarization factor does not hold experimentally.

The error estimates are calculated from the variance in intensity measurements at each position, and are typically larger for small analyzer angles. This is due to the lower average intensity at small angles, and hence the relative noise signal is higher. There are also uncertainties related to the determination of the analyzer angles, especially at small angles. These uncertainties are not included here, but are further discussed in Appendix D.1.

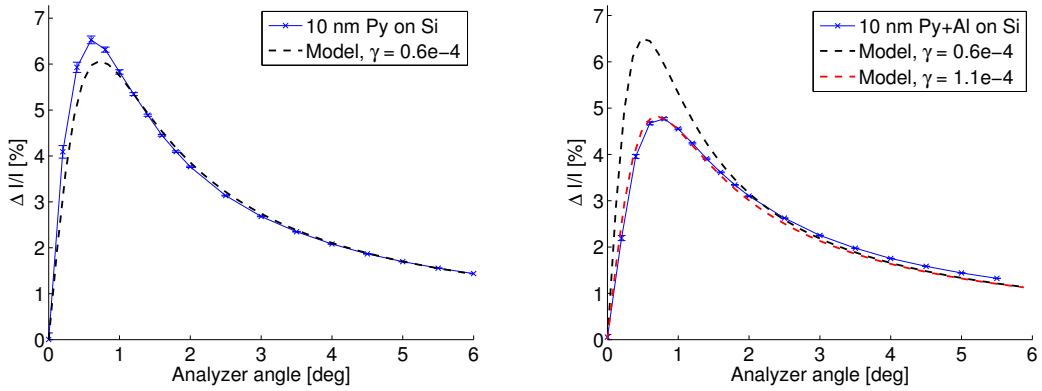

Figure 5.3: The Kerr signal contrast $\Delta I/I_{av}$ as a function of analyzer angle for P-polarized light incident on a silicon wafer coated with **(left)** a thin layer of permalloy and **(right)** a thin layer of permalloy on a 140 nm reflective aluminium layer. The experimental results are compared to modelled signal contrast curves for a 10 nm thick layer of permalloy for the two situations.

5.4 Trilayered sample 4

Fig. 5.4 shows the signal contrast $\Delta I/I_{av}$ from a silicon (100) wafer covered with a 140 nm thick totally reflecting layer of aluminium and a dielectric magnesium fluoride layer with varying thickness under a 10 nm thin film of permalloy. The experimental results are more detailed in the transition region where the thickness gradient is believed to be largest, and in the vicinity of special features in the curve, e.g. the resonance peak or the hard zero.

The MOKE signal contrast plot presented in Fig. 5.4 qualitatively resembles the modelled contrast in Fig. 5.5, where the modified value of $\gamma = 1.1 \cdot 10^{-4}$ has been used in the modelling. As can be seen from the figures, both the resonant peak at a MgF_2 thickness of approximately 210 nm, and the zero at approximately 250 nm, are easily recognized in the experimental data, though both are shifted to slightly smaller MgF_2 thicknesses. The resonance peak is sharper than the model predicts, though still clearly visible, whereas the high shoulder behind the resonance peak seems also to be shifted to smaller thicknesses.

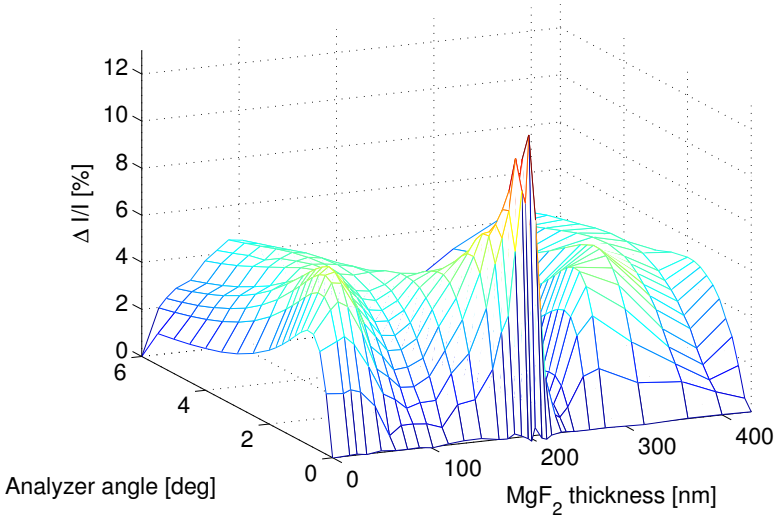

Figure 5.4: The measured MOKE signal contrast $\Delta I/I_{av}$ for P-polarized light as a function of the analyzer angle and MgF_2 underlayer thickness. The magnetic thin film is 10 nm Py on MgF_2, 140 nm Al, and a Si substrate. Maximum enhancement is observed for a MgF_2 thickness of 204 nm.

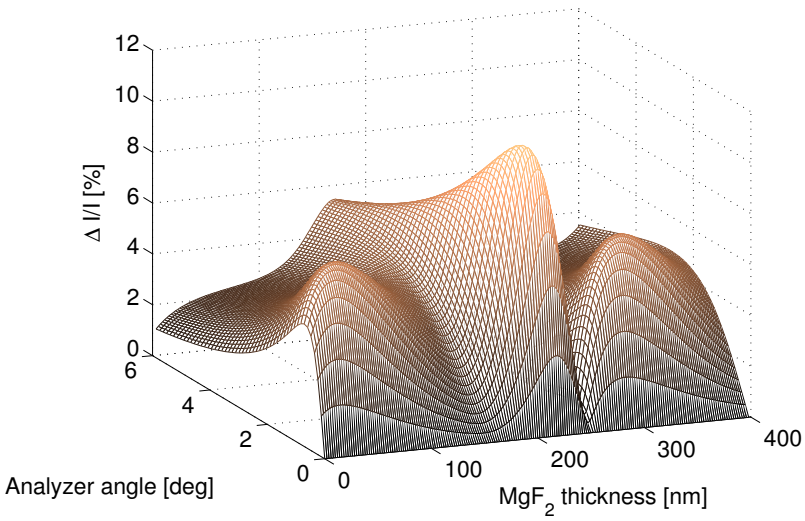

Figure 5.5: Model of the MOKE signal contrast $\Delta I/I_{av}$ for P-polarized incident light as a function of the analyzer angle and MgF_2 thickness for a 10 nm Py thin film with a MgF_2 underlayer on a 140 nm Al + Si substrate. Maximum enhancement is predicted for a MgF_2 thickness of 210 nm.

The shift of the shoulder is further visualized when comparing the maximum contrast seen experimentally with the theoretical model predictions in Fig. 5.6. Where the experimental signal contrast quickly drops to a low level for large analyzer angles, the theoretical model predicts that it should fall off with a smaller gradient.

The same position on the sample was also measured without a quarter-wave plate in the experimental setup. The model can not be fitted to the results from either of the experimental configurations by modifying the value of γ, but gives rather a prediction which is intermediate between the measured values. This suggests that the assumption of no ellipticity made in the model does not hold experimentally, and that the quarter-wave plate nulling routine does not eliminate the ellipticity of the reflected light.

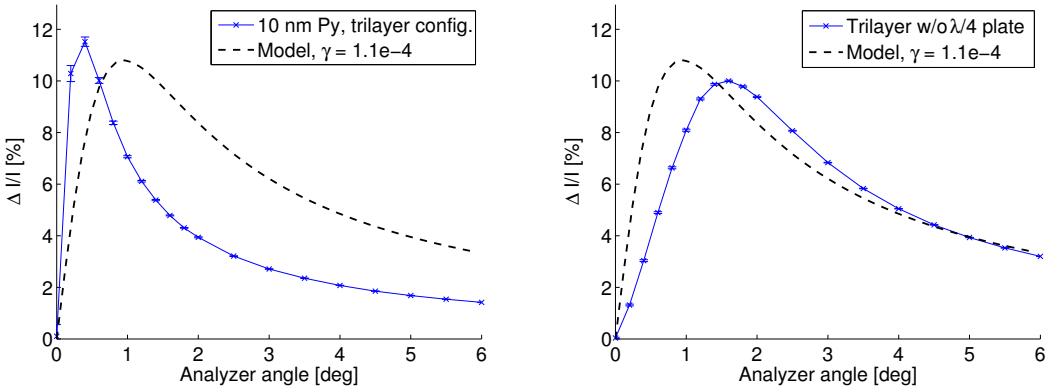

Figure 5.6: The maximum measured MOKE signal contrast $\Delta I/I_{av}$ for P-polarized light as a function of analyzer angle for 10 nm Py on a 205 nm MgF_2 + 140 nm Al underlayer. Results are shown for measurements with **(left)** and without **(right)** a quarter-wave ($\lambda/4$) plate in the experimental setup.

The maximum signal contrast measured is 11.52%, which gives an enhancement from the bare Py on Si of 1.76. Keeping a constant $\gamma = 0.6 \times 10^{-4}$ the model predicts an enhancement of 2.41. Even though the enhancement is lower than predicted by the model, the sharpness of the resonance suggests that the maximum enhancement is limited to a narrow range of thicknesses. With a large thickness gradient on the wafer surface the precise spot of maximum enhancement might be difficult to determine exactly.

5.5 Quadrilayered sample 5

The quadrilayered sample 5 was made from a silicon (100) substrate coated with a reflective layer of aluminium of approximately 140 nm. The underlayer of magnesium fluoride was deposited with a gradient in thickness, and overcoated with a thin film of 10 nm permalloy, analogous to the trilayered sample 4. Another gradient thickness layer of the high-index dielectric zinc sulphide was deposited as an anti-reflection coating on top of the permalloy film, creating a sandwiched magneto-optic quadrilayer structure. The thickness gradient of the ZnS was directed approximately perpendicular to the MgF_2 thickness gradient, creating a sample where a range of thickness combinations for the dielectric underlayer and overlayer could be measured.

For the quadrilayered configuration of sample 5, the signal contrast was seen to be highest when the quarter-wave plate was removed from the experimental setup. This is a surprising result, since the routine of iteratively minimizing the intensity by rotating the quarter wave plate and the polarization analyzer was believed to maximize the signal contrast [13]. However, it is apparent from the measurements on the quadrilayer sample that this assumption is flawed. The cause of this result is further discussed in Sec. 6.3. In the following sections, measured signal contrasts from an experimental setup without the quarter-wave plate are presented.

5.5.1 ZnS overlayer

Measurements of the contrast enhancement given by a ZnS overlayer were performed on Sample 5 in a region of low MgF_2 thickness. Fig. 5.7 shows the measured signal contrast as a function of the analyzer angle and the ZnS thickness. With only the ZnS overlayer, this is in general a trilayered configuration. However, the dielectric thickness measurements presented in Fig. 5.1 suggest that there is also a thin MgF_2 underlayer of approximately 20 nm below the Py thin film at the position of measurement on the sample. This thin MgF_2 layer is included in a modified theoretical model, presented for comparison in Fig. 5.8. In this model the modified value of $\gamma = 1.1 \times 10^{-4}$ is used, and the results are shown for the ZnS thicknesses measured experimentally.

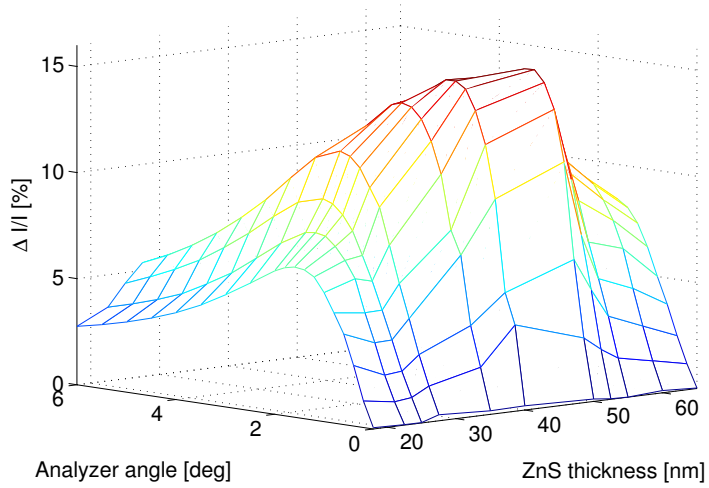

Figure 5.7: Measured signal contrast $\Delta I/I_{av}$ for P-polarized incident light without a quarter-wave plate as a function of the analyzer angle and the ZnS overlayer thickness. The configuration is a Si substrate covered with 140 nm Al, 10 nm of Py, and finally a coating of varying thickness ZnS. Maximum enhancement is observed for a ZnS thickness of 50 nm.

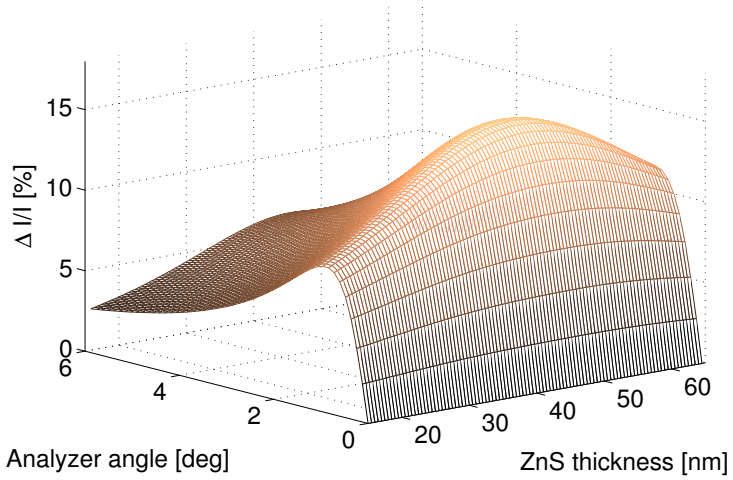

Figure 5.8: Modelled signal contrast $\Delta I/I_{av}$ for P-polarized light as a function of the analyzer angle and ZnS thickness for 10 nm Py on a 140 nm Al + Si substrate. An underlayer of 20 nm MgF_2 is included in the model since this is suggested by the thickness measurements. Maximum enhancement is predicted at a ZnS thickness of 48 nm.

Though the experimental results of Fig. 5.7 have uncertainties related to the ZnS thickness determination, it can be seen that the general shape of the curve resembles the modelled situation in Fig. 5.8. The maximum contrast is observed for a ZnS coating of 50 nm, whereas the model predicts a maximum for 48 nm ZnS.

Fig. 5.9 shows the maximum signal contrast as a function of analyzer angle measured on 10 nm Py with a ZnS anti-reflection coating. The maximum observed contrast is 15.22% for an analyzer angle of 1.2°. This is only slightly lower than the modelled contrast of 15.67%, and the modelled curve is seen to closely resemble the experimental data for a depolarization factor $\gamma = 1.1 \times 10^{-4}$. The experimental enhancement factor for the ZnS overlayer configuration is calculated to be 2.66.

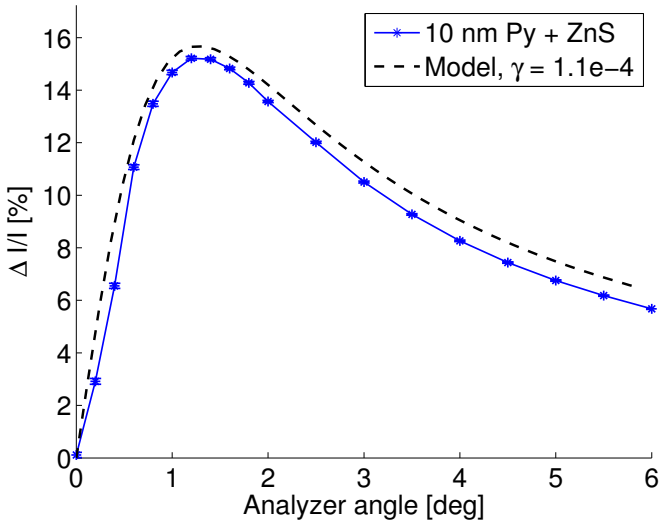

Figure 5.9: The maximum MOKE signal contrast $\Delta I/I_{av}$ for P-polarized light as a function of the analyzer angle for a sample of 10 nm Py coated with a 50 nm ZnS overlayer. A 20 nm thin layer of MgF_2 is added in the modelling to match the experimental situation.

5.5.2 Quadrilayer configuration

Since the laser beam spot size is only a few micrometres, and the region of interest on the quadrilayered sample 5, where the dielectric thicknesses vary, is of macroscopic size (approximately 10 mm x 10 mm), a complete longitudinal MOKE mapping of the surface of the sample was beyond reach in the time limit set for this project. However, a "best guess" of the ZnS thickness giving the largest total enhancement factor was performed, and the MOKE signal contrast was measured as a function of varying MgF_2 thickness.

The thickness measurements presented in Fig. 5.1 show that the ZnS thickness gradient does not reach all the way to 80 nm, which is the thickness predicted to give the largest signal contrast enhancement. However, the enhancement is predicted to be only slightly lower for a 70 nm ZnS overcoating and MgF_2 underlayer of 230 nm, a configuration which was accessible for measurement. Fig. 5.10 shows that this large predicted enhancement was not experimentally observed, measuring with or without the quarter-wave plate. At a lower ZnS thickness of approximately 53 nm, though, the sandwiched permalloy configuration showed promising results when measuring without the quarter-wave plate. These results are shown in Fig. 5.11 and compared to the modelled results at 53 nm ZnS thickness in Fig. 5.12.

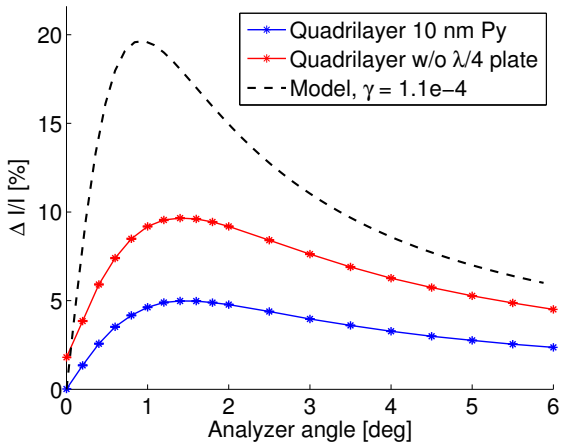

Figure 5.10: Measured MOKE signal contrast $\Delta I/I_{av}$ for P-polarized light as a function of the analyzer angle for a sample of 10 nm Py coated on top of a 230 nm MgF_2 underlayer and overcoated with a 70 nm layer of ZnS. Results are given for two experimental setups, with and without a quarter-wave ($\lambda/4$) plate. The predicted signal contrast at this thickness combination is much higher than observed experimentally.

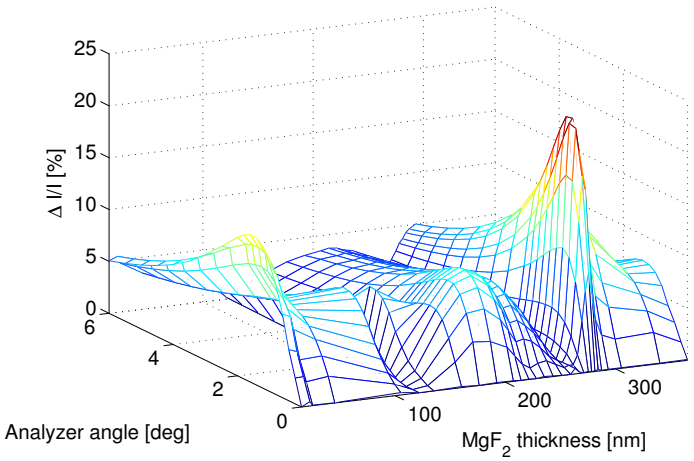

Figure 5.11: Measured MOKE signal contrast $\Delta I/I_{av}$ for P-polarized incident light without a quarter-wave plate as a function of the analyzer angle and MgF_2 thickness. The sample is a 10 nm thin film of Py, with a MgF_2 undercoating on a 140 nm Al + Si substrate, with a 53 nm ZnS overcoating. Maximum enhancement is observed for 281 nm MgF_2. The zero at 120 nm MgF_2 is believed to be caused by a vanishing Kerr rotation θ_k at this point.

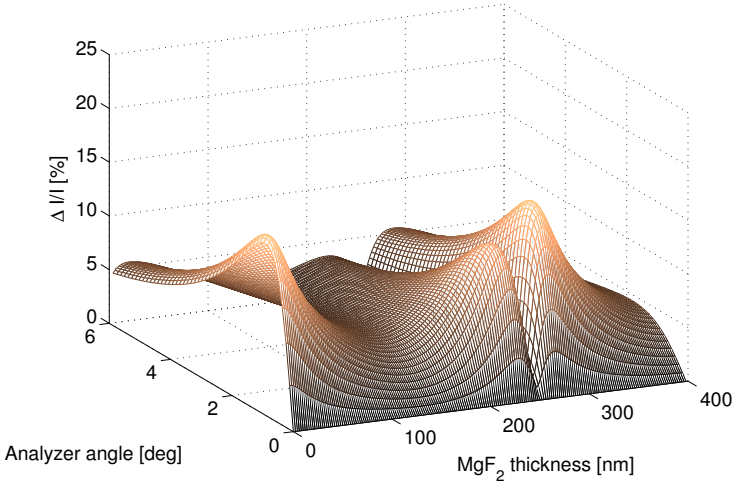

Figure 5.12: Modelled MOKE signal contrast $\Delta I/I_{av}$ for P-polarized incident light as a function of the analyzer angle and MgF_2 thickness. The modelled configuration is 10 nm Py on a variable thickness MgF_2 layer on a 140 nm Al + Si substrate. A ZnS overlayer thickness of 53 nm is included in the modelling.

Fig. 5.11 shows the signal contrast as a function of MgF_2 thickness the quadrilayered configuration of 10 nm Py on a variably thickness MgF_2 undercoating. The substrate is 140 nm Al + Si, and the ZnS overcoating thickness was measured to be approximately 53 nm. The experimental results are compared to modelling results in Fig. 5.12, for a similar quadrilayered configuration where the ZnS overlayer thickness is set to 53 nm.

The maximum signal contrast observed experimentally is 23.17%, considerably larger than the 16.53% predicted by the model with $\gamma = 1.1 \times 10^{-4}$. Compared to the signal contrast observed for a pure permalloy film on silicon from the same sample, measured to 5.72%, this represents a contrast enhancement of 4.05. Maximum enhancement is seen for a MgF_2 thickness of approximately 281 nm, whereas the model predicts a moderate signal contrast peak at 275 nm. This is within the uncertainty limits of the thickness measurements. However, the model underestimates the height of this peak substantially.

In the experimental data, a zero in the MOKE signal contrast is observed at a MgF_2 thickness of approximately 120 nm. This is not predicted by the model, and is believed to be a result of the model ignoring phase delays from the reflection components. The impact of the model's ignorance to phase differences is further discussed in Sec. 6.3.

Fig. 5.13 presents the measured I_{av} and ΔI for an analyzer angle of 1° for the quadrilayered sample. The figure shows that the high signal contrast observed at a MgF_2 thickness of 281 nm is the result of a large Kerr rotation and a small Fresnel reflection component. The modelling result of Fig. 5.12 also predicts an enhancement peak at 230 nm. Even though the experimental results of Fig. 5.13 confirm the large Kerr rotation at 230 nm, the measured $\Delta I/I_{av}$ is seen to be small at this point due to a large Fresnel reflection component. It should be noted that the value for the observed zero at a MgF_2 thickness of 120 nm is not included due to problems with accurately defining the zero angle ϕ at this point.

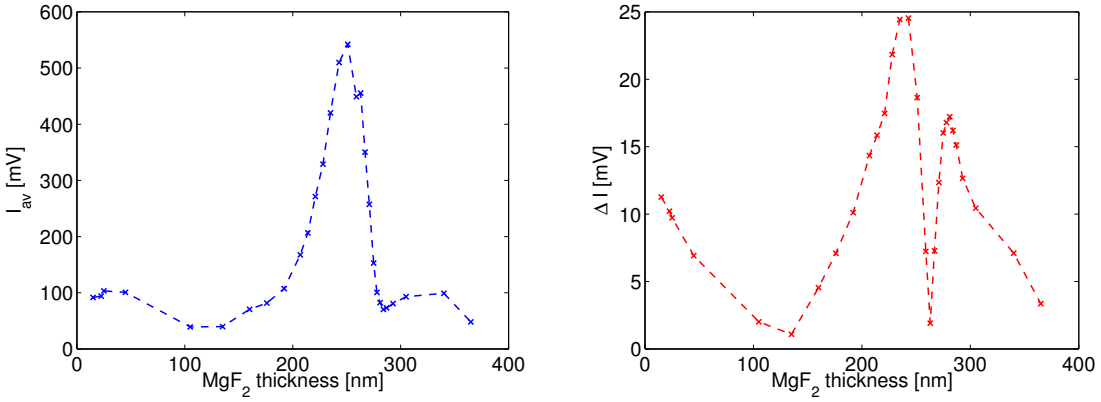

Figure 5.13: Measured I_{av} **(left)** and ΔI **(right)** at an analyzer angle $\phi = 1°$ for P-polarized incident light as a function of the MgF_2 thickness. The sample is the quadrilayered sample 5 with 10 nm Py enlosed by a varying thickness MgF_2 layer and a 53 nm ZnS layer. The substrate is Si coated with 140 nm Al. The combination of a large Kerr rotation and a small Fresnel reflectance at a MgF_2 thickness of 281 nm gives the peak in the observed signal contrast.

Chapter 6

Discussion

6.1 Signal enhancement with dielectric coatings

6.1.1 Overlayer enhancement

The experimental results shown in Sec. 5.5.1 (and in Appendix C.2) confirm that an overlayer of the high-index dielectric ZnS enhances the longitudinal MOKE signal contrast $\Delta I/I_{av}$ from a 10 nm thin film of permalloy by a factor of 2.66 for P-polarized incident light. The enhancement for S-polarized light is approximately the same. These results from a high-index dielectric overcoating are well known, and the effect has already been shown by several groups [6, 7] in the case of nickel films and magnetic nanostructures.

The dielectric overlayer enhances the Kerr signal by acting as a simple anti-reflection coating. By coupling more light into the magnetic material, a larger rotation of the polarization plane is observed. This is due to the higher ratio of the incoming light travelling into the magnetic thin film if the reflection from the surface is minimized. The surface reflection is minimized by a technique called *admittance matching* [38], where the anti-reflection coating serves to match the optical admittance of the magneto-optic layer to that of the incident medium and the substrate.

As implicitly shown by the modelling results of Fig. 3.2, the best admittance matching (e.g. that which maximizes the signal contrast) is predicted for a coating with a refractive index higher than 4. Since there are no dielectric materials with a refractive index this high which are transparent to visible light, the anti-reflection coating will not be optimized by a single-layered dielectric overlayer alone. However, it has been suggested that the admittance matching can be improved further by adding a metal thin film on top of the dielectric [6]. This metal thin film will cause

the dielectric overcoating to act like a Fabry-Perot etalon, as the light on its way back from magnetic rotation can reflect back off the top metal film, and in this way facilitate multiple Kerr reflections. This is also the principle behind the enhancement of the dielectric underlayer, described more thoroughly in the following subsections.

The advantages of a dielectric overlayer include not only direct enhancement of the Kerr signal contrast. For studies of magnetic micro- / nanostructures the overcoating can also minimize the reflectance from the substrate surrounding the magnetic structures, in this way giving a smaller noise contribution to the signal.

6.1.2 Metal covered substrate

An anti-reflection coating serves to couple the maximum amount of light into the magnetic thin film. However, it is also important to prevent the incident light from being transmitted into the substrate and lost to absorption. The absorption loss can be minimized by coating the silicon substrate with a close to totally reflecting metal coating. This will typically be a film of aluminium or gold more than 100 nm in thickness, which show reflectances of up to 90% for the wavelength used in this project [48].

When the magnetic film is deposited on top of a reflective metal layer, the light travelling all the way through the magnetic thin film is reflected off the surface of the metal, and experiences further rotation when traversing the magnetic material a second time. This effect is most visible for ultra-thin magnetic films. Magnetic materials are in general absorptive, and for thicker magnetic films only a small amount of light will reach the reflective layer, and even less escape off the surface.

A small contrast enhancement is predicted by the model when making the substrate totally reflective, even before adding dielectric coatings to the multilayer. However, this enhancement is not observed experimentally. The experimental results from 10 nm permalloy with the aluminium base layer in Fig. 5.3 show a slightly lower signal contrast than pure permalloy on silicon. The model can be modified to account for this difference if the depolarization factor γ is varied for the two situations, further weakening the view of γ as a suitable representation of the constant noise sources in the experimental setup.

Even though a single metal layer below the magnetic thin film does not enhance the signal contrast, the modelling results confirm that it is a crucial part of the trilayered dielectric underlayer configuration, as well as the quadrilayered sandwich configuration. In both these configurations the large signal contrast observed is the result of an enhanced multiple reflection effect which require a high reflectance substrate.

6.1.3 Underlayer enhancement

The results presented in Sec. 5.4 show that the longitudinal MOKE signal contrast for P-polarized light from a 10 nm thin film of permalloy can be enhanced by a factor of 1.76 by depositing the magnetic material on top of the low-index dielectric MgF_2 when the substrate has a highly reflecting Al coating. The observed enhancement is even higher for S-polarized light (Appendix C.2) and for thicker magnetic films. That a dielectric layer below the magnetic material can enhance the Kerr signal is also well known [51], and the effect relies on increasing the amount of multiple reflections off the magnetic thin film.

The dielectric underlayer acts like a Fabry-Perot etalon: The light which is transmitted through to the dielectric underlayer can continue to be reflected off the metal covered substrate and the magnetic layer, experiencing further rotation at every reflection. Whether this multiple rotation enhances or reduces the total Kerr rotation depends on the phase difference experienced inside the Fabry-Perot etalon. If the difference in optical distance traversed by the light inside and outside of the dielectric is an integer number of wavelengths, the components will add constructively, and an increased Kerr rotation is observed. On the other hand, if the multiply reflected components are out of phase with each other, the total Kerr signal may vanish for certain dielectric thicknesses.

The dielectric underlayer thicknesses giving maximum reflectance for the unrotated Fresnel and the rotated Kerr components do not in general coincide, as indirectly shown by the experimental values of ΔI and I_{av} in Fig. 5.13 for the quadrilayered sample 5. This is due to different phase changes on reflection for P-polarized and S-polarized light. This property is exploited to enhance the MOKE signal contrast: Maximum enhancement is observed where the combination of a high Kerr rotation and a low Fresnel reflectance gives a large signal contrast $\Delta I/I_{av}$.

Even though the dielectric underlayer configuration is seen to give slightly lower signal contrast enhancement than the overcoating, it still has intriguing possibilities and applications. The fact that the optical coating is deposited *below* the magnetic layer opens up the possibility to further adjust the magnetic structures after doing MOKE measurements, whereas an overcoating will not allow this. When contacting metal striplines to magnetic structures or nanowires, the underlayer can be used as an anti-reflection coating for these as well, minimizing background noise. This is important e.g. for current-induced magnetic switching applications [52, 53]. A longitudinal MOKE experimental setup is easily implemented for studying domain wall motion in magnetic micro- / nanostructures. It seems worth the effort precoating the substrate with a dielectric layer before defining the magnetic structures (e.g by electron beam lithography) if this leads to an enhancement of the useful magneto-

optical signal by a factor 2 or higher.

The sharpness of the resonance presented in Fig. 5.4 and 5.6 might present a challenge when applying a dielectric coating under magnetic micro- / nanostructures. Consequently it is crucial to be able to control the thickness of the MgF_2 coating to a precision of at least ± 5 nm to be able to exploit the maximum signal contrast enhancement. With modern deposition techniques, this should not be a problem, though.

Fig. 3.4 shows that the optimal refractive index of the Fabry-Perot layer for longitudinal MOKE is close to unity. However, making a multilayered structure where a thin film is replaced by open space is difficult, and requires state of the art photolithography and sacrificial etching techniques [54]. This configuration might also have problems with heating due to poor thermal contact with the substrate.

Due to the complexity of the experimental methods for creating open space between deposited thin films, MgF_2 seems like the most accessible low-index dielectric for future magneto-electronic devices where an enhancement of the longitudinal MOKE signal is required. However, a possible substitute is SiO_2, with only a slightly higher refractive index ($n_{SiO_2} = 1.54$ as compared to $n_{MgF_2} = 1.38$). The low refractive index of SiO_2, combined with well known deposition methods (chemical vapour deposition or sputtering techniques [55]) which produce high quality thin films with excellent thickness control, makes this material suitable for the purpose of a dielectric underlayer.

6.1.4 Quadrilayer structure

The idea of sandwiching the magneto-optic layer between a low-index dielectric underlayer and a high-index dielectric overlayer has already been shown to be useful for enhancing the *polar* MOKE for magneto-optical recording applications [56, 57, 58]. The readout of MO disks is done at normal incidence, and the effects of both the anti-reflection coating and the Fabry-Perot structure are exploited to enhance the magnetic rotation on reflection. The same optical principles can be used to describe enhancement in the longitudinal geometry, though the oblique incidence makes the modelling more complicated: The longitudinal MOKE response must be modelled separately for S- and P-polarized geometry. Both the amplitude reflection coefficients and the phase delays on reflection are generally different for these two incident polarization geometries.

The quadrilayer configuration of sample 5 combines the enhancement effects of the dielectric overlayer and underlayer: For a ZnS overcoating of 53 nm the maximum amount of light is coupled into the Fabry-Perot etalon created by the reflecting

Al layer, a MgF_2 coating, and the magnetic Py thin film. Inside the Fabry-Perot multiple reflections give a larger magnetic rotation, and interference effects are seen to enhance the measured signal contrast substantially for a MgF_2 thickness of 281 nm.

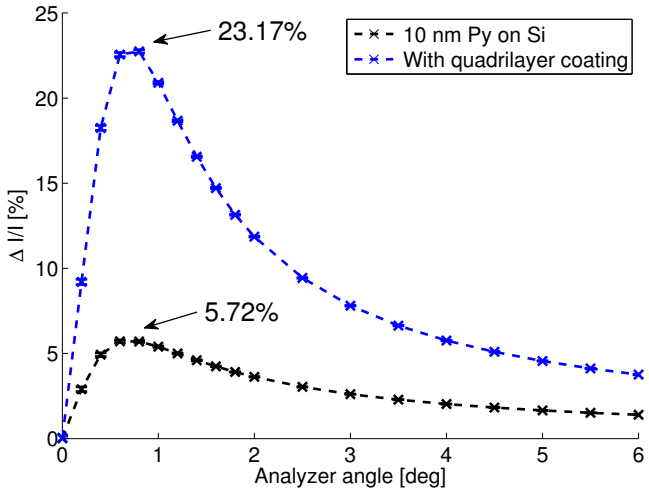

Figure 6.1: Maximum signal contrast $\Delta I/I_{av}$ for P-polarized light measured without a quarter-wave plate for the quadrilayer sample 5, where the MgF_2 thickness is 281 nm and the ZnS thickness is 53 nm. The measurements are compared to the signal contrast from a single 10 nm thin film of permalloy on a silicon substrate for the same sample. The enhancement factor is 4.05.

Fig. 6.1 shows the impact of the quadrilayer structure of sample 5 on the measured longitudinal MOKE signal contrast $\Delta I/I_{av}$. The signal from a bare permalloy thin film on silicon is enhanced a factor 4.05 for the combination of dielectric thicknesses giving maximum enhancement. This is a larger enhancement than the one reported by Cantwell et al. [6] for a ZrO_2 coated Ni thin film, and the highest signal contrast reported for longitudinal MOKE, to the best of the author's knowledge. The quadrilayer enhancement is seen to be present also for S-polarized light, and the results are reproduced for P-polarized light on a sample where Cr + Au is used as the reflecting base layer (Appendix C).

The continuous downscaling of magnetic devices brings the method of longitudinal MOKE to its resolution limits, where the structures of interest are of a size comparable to the wavelength of light. Smaller magnetic structures introduce much smaller Kerr signals than what is produced by a continuous magnetic thin film [7]. Even though the quadrilayer structure requires the ability to make multilayer stacks

of dielectric thin films with nanometre thickness precision, the reward of a substantially higher signal to noise ratio should be inviting. This is expected to be especially important for smaller magnetic structures, and crucial if the fast and non-destructive characterization technique of longitudinal MOKE is to follow into the magnetic submicrometre regime.

6.2 Longtudinal MOKE contrast

The starting point for discussing the contrast mechanisms in a longitudinal MOKE experiment is the expression for the signal contrast in Eq. 2.39. Allwood et al. [12] argue that the Kerr signal contrast $\Delta I/I_{av}$ is the figure of merit in MOKE experiments. Several groups have reported on large polar Kerr rotation angles [24, 59, 60] for multilayer combinations of magnetic, metal (with varying doping concentrations), and dielectric thin films. However, a large Kerr rotation angle might not always be the result of a large magnetic rotation on reflection. The Kerr rotation angle will also be large whenever the *unrotated* Fresnel reflection component has almost vanished. It is even theoretically possible to have Kerr components larger than the Fresnel component, and consequently Kerr rotation angles up to 90° have been reported for polar MOKE on CeSb [61, 62].

A large Kerr rotation angle can be accomplished if interference effects cause the unrotated Fresnel reflectivity to vanish completely. In longitudinal MOKE, this situation can be approximated experimentally by applying the appropriate anti-reflection coatings to magnetic thin films, though the weak signal will usually be extremely difficult to measure.

Fig. 6.2 shows a modelled situation where the Kerr rotation angle for S-polarized light is predicted to be up to 10° for a 58 nm resonance thickness of a ZnS overlayer on 13.8 nm of Py. However, the large Kerr rotation is seen to be the result of a vanishing Fresnel amplitude reflectance R_{ss}. In a situation where the Fresnel reflection component is close to eliminated, the actual signal might be too low to measure with any confidence in an experimental MOKE setup like the one described in this thesis. The noise components of the experiment are normally orders of magnitude larger than the Kerr signal, and will give large uncertainties in the measurements when the total intensity is low.

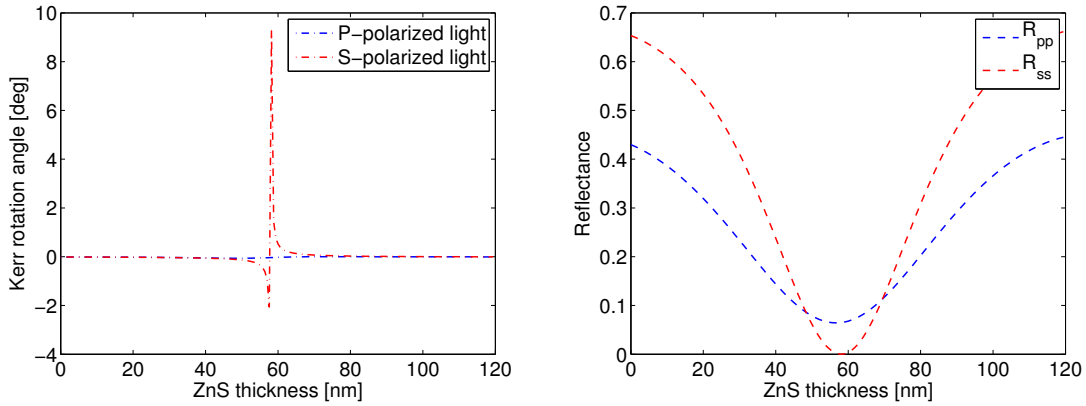

Figure 6.2: Modelled Kerr rotation angles (**left**) and Fresnel reflectance coefficients (**right**) as a function of ZnS coating thickness for 13.8 nm of Py on Si. The Kerr rotation angle for S-polarized light is very large for a ZnS overcoating of approximately 58 nm, but not experimentally accessible in a simple MOKE magnetometer setup due to the vanishing signal being lost in contributions from general noise.

On the other hand, the Kerr signal contrast $\Delta I/I_{av}$ gives a better description of the dynamic range of the Kerr signal from a magnetic thin film. In other words, the signal contrast is a better estimate of the usefulness of the signal, crucial for the ability to utilize longitudinal MOKE as a magnetic characterization technique. It is important to note that the multilayer configurations giving maximum Kerr rotation angle and Kerr signal contrast do not in general coincide, though they are usually closely related.

The experimental results in this thesis suggest that some work still remains to be able to accurately model the figure of merit $\Delta I/I_{av}$ for complex samples. The results presented in Sec. 5.5 show that Allwood's simplified formula for calculating $\Delta I/I_{av}$ partly fails in predicting the behaviour of the experimental signal contrast for a complex multilayer stack of magnetic, metal, and dielectric thin films. The predicted enhancement for a ZnS thickness of 70 nm and a MgF_2 thickness of 230 nm is not seen experimentally, whereas the strongest enhancement observed, for a ZnS thickness of 53 nm and a MgF_2 thickness of 281 nm, is not predicted by the model. These discrepancies between model and experiment are believed to be related to the phase differences of the rotated and unrotated components in a MOKE setup, introduced by the dielectric coatings on reflection.

6.3 Phase angles

The 4 x 4 matrix formalism used in the modelling of the longitudinal MOKE signal contrast includes information about the phase of the reflected components. However, the final equation calculating the MOKE *figure of merit* $\Delta I/I_{av}$, Eq. 2.40, throws away this information, and uses rather the absolute value of the field amplitudes in the expression for the signal contrast. This way of modelling the Kerr contrast is normal practice [6, 7, 12], since any phase differences between the Fresnel and Kerr components introduced on reflection are believed to be subsequently eliminated by a quarter-wave plate before the light intensity gets analyzed and detected. There are problems associated with this assumption, especially when using dielectric coatings to enhance the Kerr signal from magnetic thin films, which will be addressed in the following subsections.

6.3.1 Kerr ellipticity vs. Kerr rotation

Along with the rotation of the incident light by the magnetic thin film there generally follows a phase shift. The Kerr component is phase delayed by a factor which is dependent on the optical thickness of the media it traverses. The resulting polarization is generally elliptical, which means that the full angle of rotation cannot be measured exactly without eliminating the phase difference between the Fresnel and the Kerr components.

Fig. 6.3 shows how the polarization ellipse of the reflected light is affected by different phase delays of the Kerr component compared to the unrotated Fresnel component. The sizes of the Kerr rotation θ_k and the ellipticity ϵ_k, depend on the phase difference between the two components. Special situations are observed when the phase difference is 0°and 90°, where the ellipticity and rotation goes to zero, respectively.

Both the ellipticity and the rotation are experimentally accessible. From Eq. 2.33 it can be seen that a polarization analyzer rotated 90° with respect to the Fresnel component can be used to measure the rotation angle. If a quarter-wave plate, rotated with the fast axis along one of the reflected components and delaying the phase of the other component by $\pi/2$ (or 90°), is inserted before the analyzer, the complex Kerr angle is $i(\theta_k + i\epsilon_k) = -\epsilon_k + i\theta_k$ [4]. In this setup, the polarization analyzer, seeing only the real part of the complex rotation angle, can be used to measure the ellipticity.

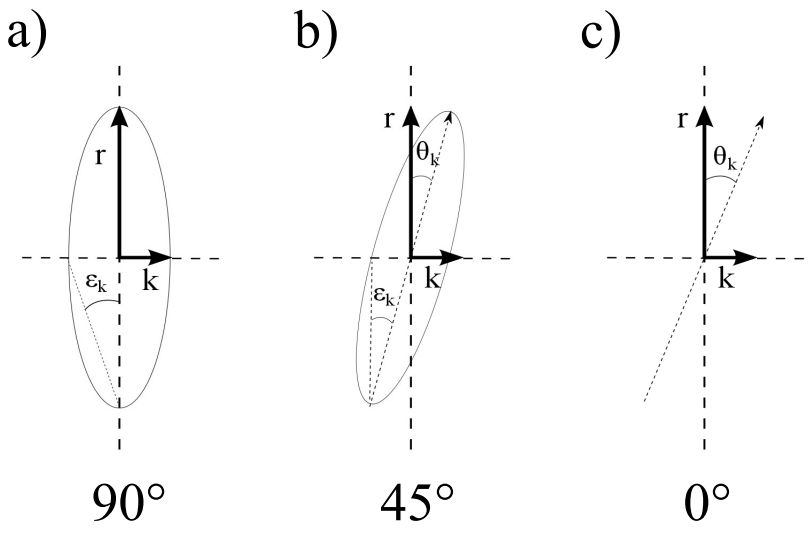

Figure 6.3: With perfect alignment, the light reflected off a magnetic thin film with magnetization in the longitudinal geometry has two different components. The unrotated Fresnel reflection **r**, and the rotated Kerr reflection **k**. The polarization of the reflected light depends on the phase difference between these two components on reflection. The resulting polarization will be **a)** elliptically polarized with ellipticity ϵ_k and zero rotation θ_k at 90° phase difference, **b)** elliptically polarized with a lower ellipticity ϵ_k and non-zero rotation θ_k at 45° phase difference, and **c)** linearly polarized with a rotation angle θ_k and no ellipticity at 0° phase difference.

6.3.2 Impact of the quarter-wave plate

The experimental setup, described in Sec. 4.2, includes a quarter wave plate in the beam path before the analyzer and detector. The motivation behind including this quarter-wave plate is to eliminate the ellipticity of the complex Kerr angle altogether, thus maximizing the accessible Kerr signal by creating linearly polarized light (situation **(c)** in Fig. 6.3). This condition is also assumed by Allwood when deriving the expression for the signal contrast $\Delta I/I_{av}$ in Eq. 2.40.

The rotation angle of the quarter-wave plate is changed for different samples and thicknesses, due to both the Kerr rotation θ_k and the Kerr ellipticity ϵ_k being largely dependent on the thicknesses and refractive indices of the dielectric coatings and the magnetic / metal layers. The optimal rotation is set manually at each sample position, following the iterative nulling procedure presented in Sec. 4.2.2.

For the quadrilayered samples, the maximum enhancement was measured without including the quarter-wave plate in the experimental setup. In fact, the measured $\Delta I/I_{av}$ at this position on the sample was seen to be dramatically lowered when following the quarter-wave plate nulling procedure. Fig. 6.4 shows how the measured maximum signal contrast for the quadrilayer sample is affected by including the quarter-wave plate.

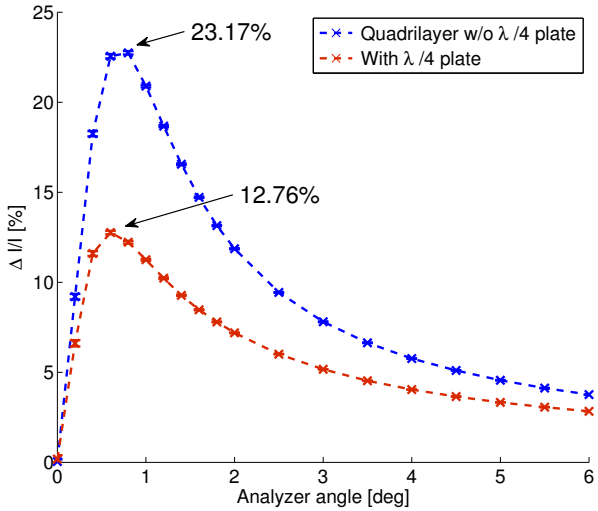

Figure 6.4: The maximum MOKE signal contrast $\Delta I/I_{av}$ for P-polarized light measured at the same position on the quadrilayer sample 5 with and without a λ/4 plate minimizing routine. Selecting only the Kerr rotation θ_k for measurement (no λ/4 plate) is seen to give a dramatically higher signal contrast at this particular point on the sample.

It is evident that the routine to minimize the detector signal by iteratively rotating the quarter-wave plate and the polarization analyzer to extinction does not maximize the Kerr signal contrast in this situation. The condition of linearly polarized light, which is an essential assumption in Allwood's model, is believed to be difficult to obtain in practice: Even if the quarter-wave plate could be accurately rotated to an angle where all ellipticity is removed from the reflected wave, the found quarter-wave plate rotation angle would not necessarily be the optimal setting when the magnetization direction switches.

6.3.3 Kerr rotation measurements

There are no experimental problems associated with removing the quarter-wave plate and measuring the signal contrast based on only the Kerr rotation θ_k. However, when using optical coatings there are usually some dielectric thicknesses where the phase of the Kerr component is delayed 90° with respect to the Fresnel component (situation **(a)** in Fig. 6.3). At these thicknesses, the measured signal contrast $\Delta I/I_{av}$ will be zero when not including a quarter-wave plate, even though the actual magnetic rotation from the sample can be substantial.

Fig. 6.5 visualizes this situation for S-polarized light incident on a modelled trilayer configuration with a ZnS overcoating and a highly reflecting Al coating on a Si substrate, similar to the one measured on sample 5. For a ZnS thickness of approximately 45 nm, the complex Kerr rotation is purely imaginary, and as a consequence no intensity modulation of the reflected light will be seen when switching magnetic field directions. This is confirmed experimentally by S-polarized measurements without a quarter-wave plate on the ZnS overcoating on sample 5, given in Fig. C.6 in Appendix C.2. The same mechanism is also believed to cause the extra zero experimentally observed at a MgF_2 thickness of 120 nm in Fig. 5.11.

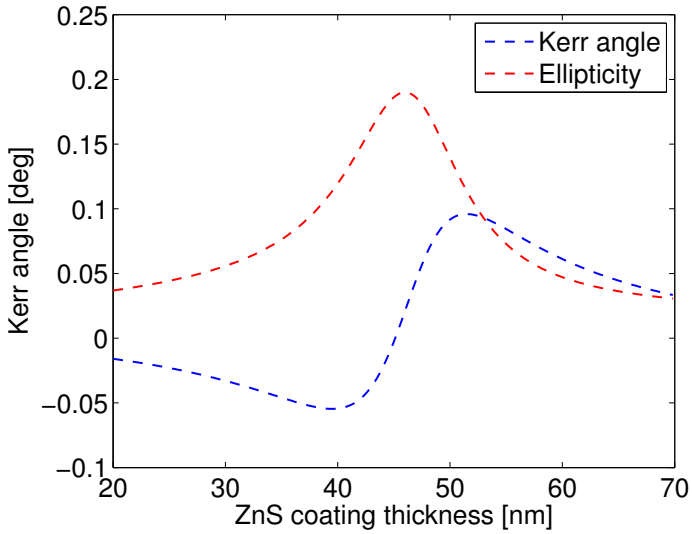

Figure 6.5: The modelled Kerr rotation θ_k and ellipticity ϵ_k for S-polarized light incident on 10 nm Py with a ZnS overcoating on a higly reflecting Al + Si substrate. θ_k changes sign at a ZnS thickness of approximately 45 nm, making measurements of the Kerr signal contrast without using a quarter-wave plate impossible.

6.3.4 Imperfect alignment

In a longitudinal MOKE experiment on magnetic thin films where optical coatings are used the amplitude of the Kerr component is typically two or three orders of magnitude smaller than than the unrotated Fresnel reflectivity. The exact ratio depends on the strength of the magnetic rotation and the amplitude reflection components of the Fresnel and Kerr components, r_{pp} and r_{ps} for P-polarized light. This typically transforms to a Kerr rotation θ_k in the interval 0.1-0.4°.

Thus Fig. 6.5 also emphasizes another important aspect with a longitudinal MOKE experiment: Only a small misalignment of the sample or the beam in the optical setup will shift the polarization of the Fresnel component a small angle away from the pure S or P configuration, and the amplitude of this small shift might still be higher than the Kerr rotation introduced by the magnetic medium. In practice, it is not possible to have an optical alignment with a level of accuracy below $\pm 0.1°$ in a simple longitudinal MOKE setup like the one described in this thesis. Experimental uncertainties, like imperfections in the polarizing beam splitter, depolarization from the focusing lenses, samples which are slightly tilted when glued to the SEM holders, and the fact that the laser light wavefronts are not perfectly planar, will all contribute to deviations from ideal optical alignment.

In the theoretical model, all deviations from ideality are collected into the depolarization constant γ in the denominator of Eq. 2.40. This term accumulates all the experimental noise contributions in one constant factor. After being introduced by Allwood et al. in 2003 [12], it has later been implemented with success by others [6, 7]. Hence γ was believed to give a good approximation to the general noise contributions in an optical setup like the one described in Sec. 4.2. However, the constant depolarization factor does not include the aspect of phase differences, which is extremely important in the case of resonant multilayer structures with optical coatings of varying thicknesses.

6.3.5 Dielectric coatings

When working with dielectric coatings to study MOKE at oblique incident angles, the phase change on reflection will generally be different for S- and P-polarized incident light. This means that a small misalignment of the incoming beam, caused by imperfections in the optical setup, results in slightly elliptically polarized reflected light. This is the case even before turning on the switching magnetic fields and including the rotated Kerr component to the resulting beam.

Fig. 6.6 shows a schematic image of the components of light reflected off a magnetic sample with a dielectric coating. In addition to the P-polarized Fresnel and

S-polarized Kerr components there is an additional S-polarized component due to alignment imperfections and depolarization effects in the optical components. This S-component is invariant to the switching of the magnetic, and hence will be called a DC offset in the following discussion (Note that the DC offset and the Kerr component are greatly exaggerated in the figure for visual purposes.).

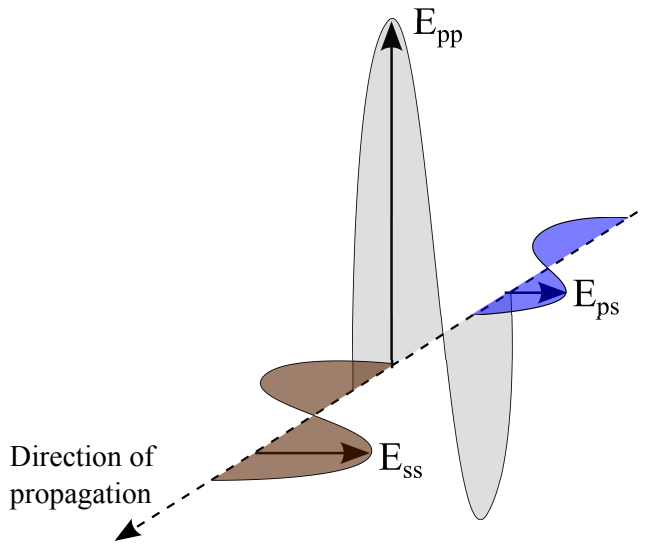

Figure 6.6: P-polarized light reflected off a magnetic thin film consists of three components: The unrotated Fresnel reflection E_{pp}, the rotated Kerr component E_{ps}, and a small component of unrotated S-polarized light E_{ss} due to alignment imperfections and depolarization in the optical components. E_{ps} and E_{ss} are greatly exaggarated in this schematic figure, though the DC offset component E_{ss} is believed to be larger than E_{ps} in most situations. For samples with dielectric coatings, the three components are in general out of phase.

This extra portion of S-polarized light in the reflected beam might have a higher amplitude than the rotated Kerr component, and when dielectric coatings are applied to the magnetic thin film, they are also in general out of phase. This means that the quarter-wave plate will not as much eliminate the ellipticity from the Kerr component as the ellipticity from the DC baseline + Kerr component combined.

Cantwell shows in his Master's thesis from 2006 [13] that rotating the quarter-wave plate away from the null-generated setting does in fact affect the signal contrast, though not lowering it more than about 2% over his range of measurement. The results obtained from the quadrilayered sample 5, presented in Sec. 5.5, suggest that this small impact of a non-optimal quarter wave plate rotation angle might have been fortuitous. In fact, removing the quarter-wave plate altogether, measuring only

the signal contrast from the Kerr rotation angle θ_k, drastically improves $\Delta I/I_{av}$ for some dielectric thicknesses.

With the results from the quadrilayer sample in mind, it can be concluded that the role of the quarter-wave plate as it is used in the experimental setup is different from its intended purpose of eliminating the ellipticity of the reflected light. The iterative quarter-wave plate nulling routine can at best select the ellipticity of the complex Kerr angle for measurement. This situation is believed to occur when the Fresnel components E_{pp} and E_{ss} are in phase. When they are out of phase, the nulling procedure will probably not select the Kerr ellipticity for measurement, but mainly act to create linearly polarized light from the elliptically polarized Fresnel reflection. At these positions on the sample, the optimal quarter-wave plate rotation angle does not coincide with the angle that gives the lowest average intensity, and is consequently much harder to find.

A question remains, however, regarding why Allwood's model is still able to give fairly good predictions for simple problems like the dielectric overcoating [6, 7], when it disregards phase differences in the calculation of $\Delta I/I_{av}$. The answer can be found in the definition of the signal contrast in Eq. 2.40: First, an important shape-determining factor when calculating $\Delta I/I_{av}$ is actually the Fresnel component E_{pp}, which is believed to be correctly represented by the 4 x 4 matrix algorithm. Second, any phase differences lowering the observed signal contrast can be accounted for by adjusting the value of the depolarization factor γ, provided the error is approximately constant for different positions on the same sample. However, for complex multilayer structures with graded layers, like the quadrilayer sample 5, the weaknesses of the model can no longer be disguised behind this presumably constant factor.

The problem of phase differences is visualized in Fig. 6.7, which presents the Fresnel phase difference (between E_{pp} and E_{ss}) and the Kerr phase difference (between E_{pp} and E_{ps}) for P-polarized light incident on both a simple ZnS overcoating and a quadrilayer structure. It is evident that the variations in phase differences are significantly more complex for a quadrilayer structure. As a consequence, the quarter-wave plate nulling routine will give unpredictable results at different dielectric thicknesses, results which can not be modelled by a varying depolarization factor alone.

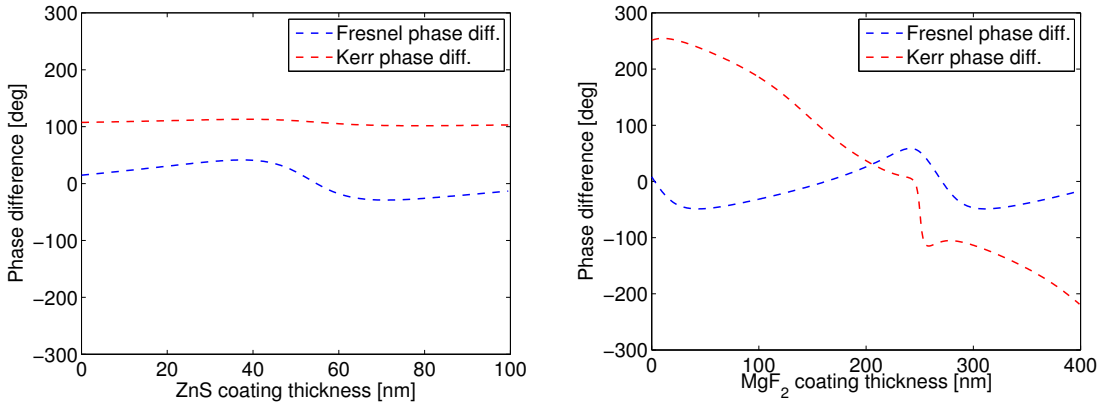

Figure 6.7: The modelled Fresnel phase difference (between E_{pp} and E_{ss}) and Kerr phase difference (between E_{pp} and E_{ps}) for P-polarized incident ligh on a ZnS overcoated Py thin film (**left**), and a quadrilayer sandwich structure (**right**) with a MgF_2 underlayer and a ZnS overlayer. The phase differences are given as a function of dielectric thickness for the two cases.

6.4 The strength of the model

Based on the experimental data obtained from the NanoMOKE^{TM}2 magnetometer, the strength of the theoretical model is discussed. It can be seen that the general trend of the experimental data are reproduced for the simpler multilayer structures. However, the model breaks down for the more complex quadrilayer samples, revealing that some assumptions made in the modelling of the signal contrast do not hold.

6.4.1 Phase considerations

The model does not include phase differences between the Fresnel and Kerr components when calculating the signal contrast. At this point, there is no reason to doubt that the 4 x 4 matrix algorithm correctly calculates both the amplitudes and the phases of the Fresnel and Kerr components after reflection off a multilayered sample. But the phase information is thrown away when calculating the actual figure of merit $\Delta I/I_{av}$. This is justified by assuming that there is no phase difference between the reflected components at the analyzer, and that all ellipticity is eliminated. However, this assumption has been shown to be incorrect, showing that a revised longitudinal MOKE model should also include information about the phases.

There should be no need for making the assumption of linearly polarized light in the first place. A quarter-wave plate and a polarization analyzer are simple optical

components which can be included directly in the modelling through their Jones matrix elements [37]. In this way the actual intensity hitting the photodetector can be modelled as a function of the rotation angle of the quarter-wave plate and the analyzer, and the optimal combination can be found.

6.4.2 The depolarization factor

Even though the constant depolarization factor γ might be a good approximation to noise contributions from samples with a high degree of homogeneity, this is not the case for a sample with two perpendicularly oriented dielectric thickness gradients. The depolarization constant assumes that the noise elements in the reflected light originate from imperfections in the optical setup alone, disregarding the fact that the sample itself can reduce or amplify the DC offset component, e.g. due to surface scattering. Furthermore, the contribution from the DC offset can also vary within one sample, e.g. for a sample where the thickness of one or more of the layers in a multilayer stack are varying.

To accurately model the DC offset term from complex structures like the quadri-layered sample 5 in this experiment might at first seem like a problematic task. However, the problem simplifies if the quarter-wave plate is removed from the experimental setup. In this case the noise analysis reduces to a determination of the component E_{ss} in Fig. 6.6, since the noise contributions in the P direction (still focusing on P-polarized incident light) are believed to be very small compared to the signal strength. Other unpolarized noise sources might still be modelled with a constant like γ, since they originate from the surroundings and imperfections in the optical components, and are likely to have phase factors which are either random or independent of the measurement position on the sample.

Nevertheless, the major noise term contributing to I_{av} should be the small fraction of S-polarized incident light E_{ss} originating from alignment imperfections. When estimating the value of this component it is crucial to include the variations in the Fresnel reflection amplitudes for different dielectric thicknesses, as well as the phase delays obtained on reflection.

Chapter 7

Conclusion

The most important results from the study of optical coatings for the enhancement of the longitudinal magneto-optic Kerr effect from ultra-thin magnetic films can be summarized:

- A signal contrast enhancement of a factor 1.76 is observed for P-polarized light on a trilayer configuration of 10 nm permalloy with a magnesium fluoride underlayer and a 140 nm aluminium reflective base layer. The maximum enhancement is seen for a MgF_2 thickness of 205 nm.

- The enhancement from the dielectric underlayer is also visible using S-polarized incident light, and the results are reproduced for samples using 20 nm permalloy, 20 nm nickel, and 10 nm nickel as the magnetic layer.

- A signal contrast enhancement of a factor 4.05 is observed for P-polarized light on a quadrilayer configuration where an additional anti-reflection coating of zinc sulphide is applied to the trilayer configuration. Maximum enhancement is observed without using a quarter-wave plate in the optical setup. The optimal dielectric thicknesses were found to be 53 nm for the ZnS overlayer, and 281 nm for the MgF_2 underlayer.

- The enhancement from the quadrilayer configuration is also visible using S-polarized incident light, and the results are reproduced for a sample where gold is used as the reflecting base layer.

- The simplified model used to calculate the MOKE signal contrast $\Delta I/I_{av}$, as defined by Allwood et al. [12], does not give an adequate prediction for complex samples.

- The inaccuracy of the model is believed to be a result of the phase factors of the reflected components being ignored when calculating the signal contrast. The discrepancy between model and experimental data is more pronounced for complex multilayer structures where the variations in phase factors are larger.

7.1 Further work

The natural next step in the development of optical coatings for longitudinal MOKE is to apply the quadrilayer configuration to smaller magnetic structures, down to the submicrometre regime. This would challenge the concepts of Kerr rotation enhancement when the total signal is small.

The quarter-wave plate and the polarization analyzer should be included in the model in the form of matrix elements to give a more accurate description of the experimental setup. In addition the model should be modified to account for the phase differences between the different reflected components.

Bibliography

[1] S. A. Wolf, D. D. Awschalom, R. A. Buhrman, J. M. Daughton, S. von Molnár, M. L. Roukes, A. Y. Chtchelkanova, and D. M. Treger. Spintronics: A spin-based electronics vision for the future. *Science*, 294(5546):1488–1495, 2001.

[2] David D. Awshcalom and Michal E. Flatte. Challenges for semiconductor spintronics. *Nature Physics*, 3(3):153–159, 2007.

[3] Del Atkinson, Dan A. Allwood, Ganga Xiong, Michael D. Cooke, Colm C. Faulkner, and Russel P. Cowburn. Magnetic domain-wall dynamics in a submicrometre ferromagnetic. *Nat Mater*, 2:85–87, 2003.

[4] Z. Q. Qiu and S. D. Bader. Surface magneto-optic kerr effect. *Review of Scientific Instruments*, 71(3):1243–1255, 2000.

[5] R. P. Cowburn. Property variation with shape in magnetic nanoelements. *Journal of Physics D: Applied Physics*, 33(1):R1, 2000.

[6] P. R. Cantwell, U. J. Gibson, D. A. Allwood, and H. A. M. Macleod. Optical coatings for improved contrast in longitudinal magneto-optic kerr effect measurements. *Journal of Applied Physics*, 100(9), 2006.

[7] U. J. Gibson, L. F. Holiday, D. A. Allwood, S. Basu, and P. W. Fry. Enhanced longitudinal magnetooptic kerr effect contrast in nanomagnetic structures. *IEEE Transactions on Magnetics*, 43(6):2740–2742, june 2007.

[8] D. A. Allwood, G. Xiong, C. C. Faulkner, D. Atkinson, D. Petit, and R. P. Cowburn. Magnetic domain-wall logic. *Science*, 309(5741):1688–1692, 2005.

[9] S. R. Bowden and U. J. Gibson. Optical characterization of all-magnetic NOT gate operation in vortex rings. *Magnetics, IEEE Transactions on*, 45(12):5326–5332, 2009.

[10] I. Abdulhalim. Analytic propagation matrix method for linear optics of arbitrary biaxial layered media. *Journal of Optics A: Pure and Applied Optics*, 1(5):646, 1999.

[11] I. Abdulhalim. Analytic propagation matrix method for anisotropic magneto-optic layered media. *Journal of Optics A: Pure and Applied Optics*, 2(6):557, 2000.

[12] D. A. Allwood, Gang Xiong, M. D. Cooke, and R. P. Cowburn. Magneto-optical Kerr effect analysis of magnetic nanostructures. *Journal of Physics D: Applied Physics*, 36(18):2175, 2003.

[13] Patrick R. Cantwell. Optical coatings for improved contrast in longitudinal magneto-optic kerr effect (MOKE) measurements. Master's thesis, Thayer School of Engineering, Darthmouth College, Hanover, New Hampshire, 2006.

[14] D. Chen, J. F. Ready, and E. Bernal G. MnBi thin films: Physical properties and memory applications. *Journal of Applied Physics*, 39(8):3916–3927, 1968.

[15] S Tsunashima. Magneto-optical recording. *Journal of Physics D: Applied Physics*, 34(17):R87, 2001.

[16] Rainer Waser. *Nanoelectronics and Information Technology*. Wiley-VCH, Weinheim, Germany, 2nd edition, 2005.

[17] B. N. Engel, N. D. Rizzo, J. Janesky, J. M. Slaughter, R. Dave, M. DeHerrera, M. Durlam, and S. Tehrani. The science and technology of magnetoresistive tunneling memory. *Nanotechnology, IEEE Transactions on*, 1(1):32–38, mar 2002.

[18] R. P. Cowburn and M. E. Welland. Room temperature magnetic quantum cellular automata. *Science*, 287(5457):1466–1468, 2000.

[19] A. Imre, G. Csaba, L. Ji, A. Orlov, G. H. Bernstein, and W. Porod. Majority logic gate for magnetic quantum-dot cellular automata. *Science*, 311(5758):205–208, 2006.

[20] B. Terris, T. Thomson, and G. Hu. Patterned media for future magnetic data storage. *Microsystem Technologies*, 13:189–196, 2007.

[21] P. Kasiraj, R. Shelby, J. Best, and D. Horne. Magnetic domain imaging with a scanning Kerr effect microscope. *Magnetics, IEEE Transactions on*, 22(5):837–839, sep 1986.

[22] E. Betzig, J. K. Trautman, R. Wolfe, E. M. Gyorgy, P. L. Finn, M. H. Kryder, and C.-H. Chang. Near-field magneto-optics and high density data storage. *Applied Physics Letters*, 61(2):142–144, 1992.

[23] T. J. Silva, S. Schultz, and Dieter Weller. Scanning near-field optical microscope for the imaging of magnetic domains in optically opaque materials. *Applied Physics Letters*, 65(6):658–660, 1994.

[24] N. Qureshi, H. Schmidt, and A. R. Hawkins. Cavity enhancement of the magneto-optic kerr effect for optical studies of magnetic nanostructures. *Applied Physics Letters*, 85(3):431–433, 2004.

[25] Naser Qureshi, Suqin Wang, Mark A. Lowther, Aaron R. Hawkins, Sunghoon Kwon, Alexander Liddle, Jeffrey Bokor, and Holger Schmidt. Cavity-enhanced magnetooptical observation of magnetization reversal in individual single-domain nanomagnets. *Nano Letters*, 5(7):1413–1417, 2005.

[26] Chun-Yeol You and Sung-Chul Shin. Generalized analytic formulae for magneto-optical kerr effects. *Journal of Applied Physics*, 84(1):541–546, 1998.

[27] J. Kranz and W. Drechsel. Über die Beobachtung von Weißschen Bereichen in polykristallinem Material durch die vergrößerte magneto-optische Kerrdrehung. *Zeitschrift für Physik A Hadrons and Nuclei*, 150(5):632–639, 1958.

[28] K. Balasubramanian, A. S. Marathay, and H. A. Macleod. Modeling magneto-optical thin film media for optical data storage. *Thin Solid Films*, 164:391–403, 1988.

[29] R. Atkinson, I. W. Salter, and J. Xu. Quadrilayer magneto-optic enhancement with zero Kerr ellipticity. *Journal of Magnetism and Magnetic Materials*, 102(3):357–364, 1991.

[30] R. Atkinson. Design of magneto-optic phase-optimised tri-layer systems for the enhancement of the polar Kerr effect. *Journal of Magnetism and Magnetic Materials*, 124(1-2):178–184, 1993.

[31] Pochi Yeh. Optics of anisotropic layered media: A new 4 x 4 matrix algebra. *Surface Science*, 96(1-3):41–53, 1980.

[32] M. Mansuripur. Analysis of multilayer thin-film structures containing magneto-optic and anisotropic media at oblique incidence using 2 x 2 matrices. *Journal of Applied Physics*, 67(10):6466–6475, 1990.

[33] J. Zak, E. R. Moog, C. Liu, and S. D. Bader. Magneto-optics of multilayers with arbitrary magnetization directions. *Phys. Rev. B*, 43(8):6423–6429, Mar 1991.

[34] D. A. Allwood, Gang Xiong, M. D. Cooke, C. C. Faulkner, D. Atkinson, N. Vernier, and R. P. Cowburn. Submicrometer ferromagnetic not gate and shift register. *Science*, 296(5575):2003–2006, 2002.

[35] J. Rothman, M. Kläui, L. Lopez-Diaz, C. A. F. Vaz, A. Bleloch, J. A. C. Bland, Z. Cui, and R. Speaks. Observation of a bi-domain state and nucleation free switching in mesoscopic ring magnets. *Phys. Rev. Lett.*, 86(6):1098–1101, Feb 2001.

[36] S. R. Bowden, K. K. L. Ahmed, and U. J. Gibson. Longitudinal magneto-optic Kerr effect detection of latching vortex magnetization chirality in individual mesoscale rings. *Applied Physics Letters*, 91(23), 2007.

[37] B. E. A. Saleh and M. C. Teich. *Fundamentals of Photonics*. John Wiley and Sons, Inc., 2nd edition, 2007.

[38] H. Angus Macleod. *Thin Film Optical Filters*. CRC Press, Taylor and Francis Group, 4th edition, 2010.

[39] Lukas Novotny and Bert Hecht. *Principles of nano-optics*. Cambridge University Press, 2nd edition, 2007.

[40] E. Hecht. *Optics*. Addison-Wesley Publishing Company, 2nd edition, 1987.

[41] C Fabry and A Perot. Theorie et applications d'une nouvelle méthode de spectroscopie interférentielle. *Annales des Chimie et des Physique*, 6(16):115–144, 1899.

[42] W. Voigt. *Handbook der Elektrizitat und des Magnetismus*, volume IV. Barth, Leipzig, 1915.

[43] John Kerr. On rotation of the plane of polarization by reflection from the pole of a magnet. *Philosophical Magazine Series*, 3:321, 1877.

[44] John Kerr. On reflection of polarized light from the equatorial surface of a magnet. *Philosophical Magazine Series*, 5:161, 1878.

[45] P. B. Johnson and R. W. Christy. Optical constants of transition metals: Ti, V, Cr, Mn, Fe, Co, Ni, and Pd. *Phys. Rev. B*, 9(12):5056–5070, Jun 1974.

[46] S. Visnovsky, V. Parízek, M. Nyvlt, P. Kielar, V. Prosser, and R. Krishnan. Magneto-optical Kerr spectra of nickel. *Journal of Magnetism and Magnetic Materials*, 127(1-2):135–139, 1993.

[47] A. Berger and M. R. Pufall. Generalized magneto-optical ellipsometry. *Applied Physics Letters*, 71(7):965–967, 1997.

[48] Edward D. Palik. *Handbook of optical constants of Solids*, volume I-IV. Academic Press, 2nd edition, 1998.

[49] Leon I. Maissel and Reinhard Glang. *Handbook of Thin Film Technology*, volume I. McGraw-Hill Book Company, 1970.

[50] Gesche Nahrwold, Jan M. Scholtyssek, Sandra Motl-Ziegler, Ole Albrecht, Ulrich Merkt, and Guido Meier. Structural, magnetic, and transport properties of permalloy for spintronic experiments. *Journal of Applied Physics*, 108(1), 2010.

[51] D. Keay and P. H. Lissberger. Longitudinal Kerr magneto-optic effect in multilayer structures of dielectric and magnetic films. *Optica Acta: International Journal of Optics*, 15(4):373–388, 1968.

[52] N. Vernier, D. A. Allwood, D. Atkinson, M. D. Cooke, and R. P. Cowburn. Domain wall propagation in magnetic nanowires by spin-polarized current injection. *EPL (Europhysics Letters)*, 65(4):526, 2004.

[53] M. Yamanouchi, D. Chiba, F. Matsukura, and F. Ohno. Current-induced domain-wall switching in a ferromagnetic semiconductor structure. *Nature*, 428(6982):539–542, 2004.

[54] Yang-Kyu Choi, Tsu-Jae King, and Chenming Hu. A spacer patterning technology for nanoscale CMOS. *Electron Devices, IEEE Transactions on*, 49(3):436 –441, mar 2002.

[55] Michael Quirk and Julian Serda. *Semiconductor Manufacturing Technology*. Prentice Hall, Inc., 1st edition, 2001.

[56] M. Mansuripur, G. Connell, and D. Treves. Optimum disk structures and energetics of domain formation in magneto-optical recording. *Magnetics, IEEE Transactions on*, 18(6):1241–1243, nov 1982.

[57] R. Gamble, P. Lissberger, and M. Parker. A simple analysis for the optimization of the normal polar magneto-optical Kerr effect in multilayer coatings containing a magnetic film. *Magnetics, IEEE Transactions on*, 21(5):1651–1653, sep 1985.

[58] Masud Mansuripur. *The physical principles of magneto-optical recording*. Cambridge University Press, 1st edition, 1998.

[59] K. Nakamura, T. Asaka, S. Asari, Y. Ota, and A. Itoh. Enhancement of Kerr rotation with amorphous Si film. *Magnetics, IEEE Transactions on*, 21(5):1654–1656, sep 1985.

[60] Y. J. Wang, Z. H. Guo, D. K. Zhu, and C. H. Shang. Kerr rotation enhancement and correlation between perpendicular anisotropy and Kerr effect in PtCu(Al,Ag)/Co multilayers. *Journal of Applied Physics*, 80(7):3957–3961, oct 1996.

[61] R. Pittini, J. Schoenes, O. Vogt, and P. Wachter. Discovery of 90 degree magneto-optical polar Kerr rotation in CeSb. *Phys. Rev. Lett.*, 77(5):944–947, Jul 1996.

[62] A. N. Yaresko, P. M. Oppeneer, A. Ya. Perlov, V. N. Antonov, T. Kraft, and H. Eschrig. On the nature of the absolute maximal observable magneto-optical Kerr rotation of CeSb. *EPL (Europhysics Letters)*, 36(7):551, 1996.

[63] G. S. Krinchik and V. A. Artemjev. Magneto-optic properties of nickel, iron, and cobalt. *Journal of Applied Physics*, 39(2):1276–1278, 1968.

[64] G. Neuber, R. Rauer, J. Kunze, T. Korn, C. Pels, G. Meier, U. Merkt, J. Backstrom, and M. Rubhausen. Temperature-dependent spectral generalized magneto-optical ellipsometry. *Applied Physics Letters*, 83(22):4509–4511, 2003.

[65] D. Stroud. Generalized effective-medium approach to the conductivity of an inhomogeneous material. *Phys. Rev. B*, 12(8):3368–3373, Oct 1975.

Appendix A

The 4x4 matrix method

This section summarizes the most important results from Abdulhalim's 4 x 4 matrix formulation for general magneto-optical media, which has been applied in the modelling of the longitudinal magneto-optical Kerr effect response from a multilayer stack [10, 11].

Considering a medium free of sources and homogeneous in the xy plane, the wave functions for the complex electric and magnetic fields can be expressed as

$$\begin{aligned} \mathbf{E}(r,t) &= \mathbf{E}(z)e^{i(\mathbf{k}\cdot\mathbf{r}-\omega t)} \\ \mathbf{H}(r,t) &= \mathbf{H}(z)e^{i(\mathbf{k}\cdot\mathbf{r}-\omega t)} \end{aligned} \tag{A.1}$$

where $\mathbf{k} = k_x\hat{x} + k_y\hat{y} + k_z\hat{z}$ is the propagation vector, and ω being the optical frequency.

Fig. A.1 shows the general geometry of an electromagnetic wave incident on an arbitrarily biaxial medium. Abdulhalim relates the propagation vector to a characteristic direction vector through $\mathbf{k} = k_0(\nu_x, \nu_y, \nu_z)$, where $k_0 = 2\pi/\lambda_0$ is the wavenumber of free space. The characteristic direction vector ν is related to the refractive indices of the two media through

$$\nu_{1,2} = n_{1,2}(\sin\gamma_{1,2}\cos\phi, \sin\gamma_{1,2}\sin\phi, \cos\gamma_{1,2}) \tag{A.2}$$

where $\gamma_{1,2}$ and ϕ are the polar and azimuth angles of incidence of the wave, represented in Fig. A.1.

In the 4×4 matrix approach the components of the electric and magnetic fields are arranged in a column form

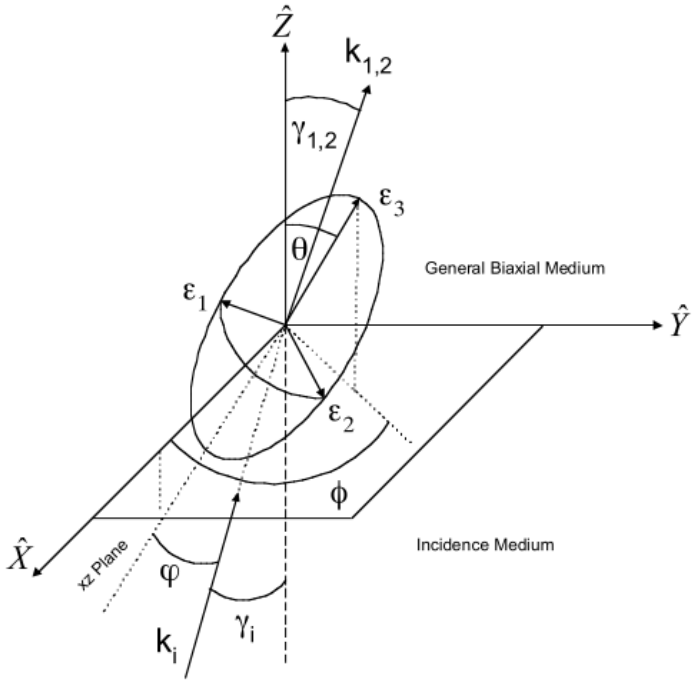

Figure A.1: General geometry of an electromagnetic wave incident on the surface of a general biaxial medium [10].

$$\Psi = \begin{pmatrix} \sqrt{\epsilon_0} E_x \\ \sqrt{\mu_0} H_y \\ \sqrt{\epsilon_0} E_y \\ -\sqrt{\mu_0} H_x \end{pmatrix} \tag{A.3}$$

where the electric and magnetic fields are given as perpendicular and parallel to the interface. This arrangement opens up the possibility to write Maxwell's equations in the form of a first-order system of differential equations

$$\frac{\partial \Psi}{\partial z} = i k_0 \Delta \Psi \ . \tag{A.4}$$

By a proper choice of coordinate system, the xz plane can always be chosen as the

plane of incidence, and the Δ-matrix can be described as

$$\Delta = \begin{pmatrix} -\nu_x\epsilon_{zx}/\epsilon_{zz} & 1-\nu_x^2/\epsilon_{zz} & -\nu_x\epsilon_{zy}/\epsilon_{zz} & 0 \\ \epsilon_{xx}-\epsilon_{xz}\epsilon_{zx}/\epsilon_{zz} & -\nu_x\epsilon_{xz}/\epsilon_{zz} & \epsilon_{xy}-\epsilon_{xz}\epsilon_{zy}/\epsilon_{zz} & 0 \\ 0 & 0 & 0 & 1 \\ \epsilon_{yx}-\epsilon_{yz}\epsilon_{zx}/\epsilon_{zz} & -\nu_x\epsilon_{yz}/\epsilon_{zz} & \epsilon_{yy}-\nu_x^2-\epsilon_{yz}\epsilon_{zy}/\epsilon_{zz} & 0 \end{pmatrix}. \tag{A.5}$$

For longitudinal MOKE geometry, the magnetic field is applied in the plane of incidence, e.g. the x direction, giving a simpler expression for the dielectric tensor in Eq. 2.31

$$\hat{\epsilon} = \epsilon \begin{pmatrix} 1 & 0 & 0 \\ 0 & 1 & iQ_x \\ 0 & -iQ_x & 1 \end{pmatrix} \tag{A.6}$$

for a medium with $\epsilon_{xx} = \epsilon_{yy} = \epsilon_{zz} = \epsilon$, where Q_x depends on the *optical activity* of the magnetic medium. With this experimental geometry, Eq. A.5 simplifies to

$$\Delta = \begin{pmatrix} 0 & 1-\nu_x^2/\epsilon_{zz} & -\nu_x\epsilon_{zy}/\epsilon_{zz} & 0 \\ \epsilon_{xx} & 0 & 0 & 0 \\ 0 & 0 & 0 & 1 \\ 0 & -\nu_x\epsilon_{yz}/\epsilon_{zz} & \epsilon_{yy}-\nu_x^2-\epsilon_{yz}\epsilon_{zy}/\epsilon_{zz} & 0 \end{pmatrix}. \tag{A.7}$$

The general solution to equation A.4 is a wavefunction of the form

$$\Psi(z+h) = e^{ihk_o\Delta}\Psi_0(z) \tag{A.8}$$

where h is the distance travelled within the homogeneous medium characterized by the Δ-matrix. The matrix

$$P(h) = e^{ihk_0\Delta} \tag{A.9}$$

is called the *transfer matrix* or the *propagation matrix* of the system, and can be calculated by solving the eigenvalues of the Δ-matrix. See [10] for details.

For the isotropic case, e.g. a dielectric medium, the 4 x 4 matrix approach simplifies drastically, and the eigenvalues of the Δ-matrix can be calculated as $\nu_{z1,3} = \pm\sqrt{\epsilon-\nu_x^2}$, where ϵ is the isotropic dielectric constant. The propagation matrix is then given by

$$P = \begin{pmatrix} \cos(k_0 h\nu_{z1}) & \frac{i\nu_{z1}\sin(k_0 h\nu_{z1})}{\epsilon} & 0 & 0 \\ \frac{i\epsilon\sin(k_0 h\nu_{z1})}{\nu_{z1}} & \cos(k_0 h\nu_{z1}) & 0 & 0 \\ 0 & 0 & \cos(k_0 h\nu_{z1}) & \frac{i\sin(k_0 h\nu_{z1})}{\nu_{z1}} \\ 0 & 0 & i\nu_{z1}\sin(k_0 h\nu_{z1}) & \cos(k_0 h\nu_{z1}) \end{pmatrix} . \quad \text{(A.10)}$$

If the propagation matrix of each layer in a multilayer stack is known, the total propagation matrix of the system can easily be calculated. If each layer $j = 1, 2, \ldots N$ in a multilayer stack is characterized by a propagation matrix P_j, the total propagation matrix is given by the matrix product

$$P = P_N P_{N-1} \ldots P_j \ldots P_1 \ . \quad \text{(A.11)}$$

The tangential field components at the two interfaces defined by the layers in the propagation matrix must be matched, elegantly described by the requirement

$$\Psi_t = P(\Psi_i + \Psi_r) \quad \text{(A.12)}$$

where Ψ_i, Ψ_r, and Ψ_t are the incident, reflected, and transmitted components of the incident wavefunction, respectively. From Eq. A.12 the reflection components of Eq. 2.34 can be calculated directly as

$$\mathbf{r} = \begin{pmatrix} r_{ss} & r_{ps} \\ r_{sp} & r_{pp} \end{pmatrix} = \frac{1}{(a_4 a_6) - a_2 a_8)} \begin{pmatrix} a_1 a_8 - a_4 a_5 & a_3 a_8 - a_4 a_7 \\ a_2 a_5 - a_1 a_6 & a_2 a_7 - a_6 a_3 \end{pmatrix} \quad \text{(A.13)}$$

where a_j are calculated from the P-matrix, the angle of incidence and transmission γ_i and γ_t, and the refractive indices of the incidence and substrate media, n_i and n_t:

$$\begin{aligned} a_{1,2} &= n_i(n_t P_{12} - \cos\gamma_i P_{22}) \pm \cos\gamma_t(n_t P_{11} - \cos\gamma_t P_{21}) \\ a_{3,4} &= (n_t P_{13} - \cos\gamma_i P_{23}) \pm n_i \cos\gamma_t(n_t P_{14} - \cos\gamma_t P_{24}) \\ a_{5,6} &= n_i(n_t \cos\gamma_t P_{32} - P_{42}) \pm \cos\gamma_i(n_t \cos\gamma_t P_{31} - P_{41}) \\ a_{7,8} &= (n_t \cos\gamma_t P_{33} - P_{43}) \pm n_i \cos\gamma_i(n_t \cos\gamma_t P_{34} - P_{44}) \ . \end{aligned} \quad \text{(A.14)}$$

When the reflection coefficients of Eq. A.13 are established, the electric field components for the S- and P-polarized geometry are calculated from Eq. 2.34. The signal contrast $\Delta I/I_{av}$ is given by assuming linearly polarized light and using the absolute values of the electric fields in Eq. 2.40.

Appendix B

S-polarized modelling results

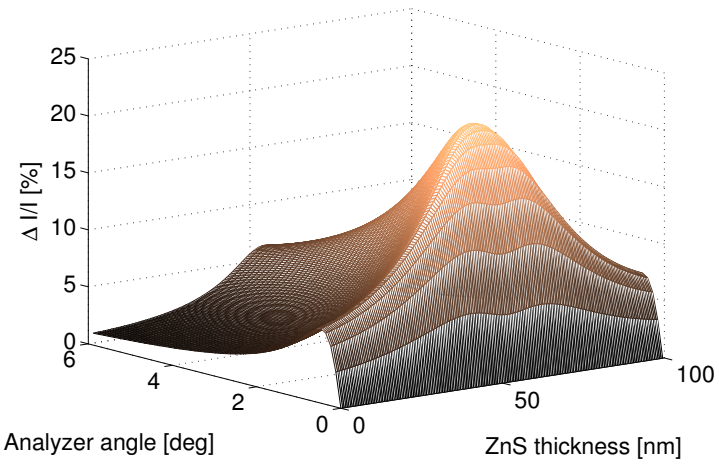

Figure B.1: Modelled signal contrast $\Delta I/I_{av}$ for S-polarized incident light as a function of analyzer angle and ZnS overcoating thickness. The magneto-optical layer is a 10 nm thick layer of Py, coated on top of a Si substrate coated with 100 nm Al. The dielectric overlayer is a variable thickness ZnS layer. Maximum enhancement is predicted at a ZnS thickness of 53 nm.

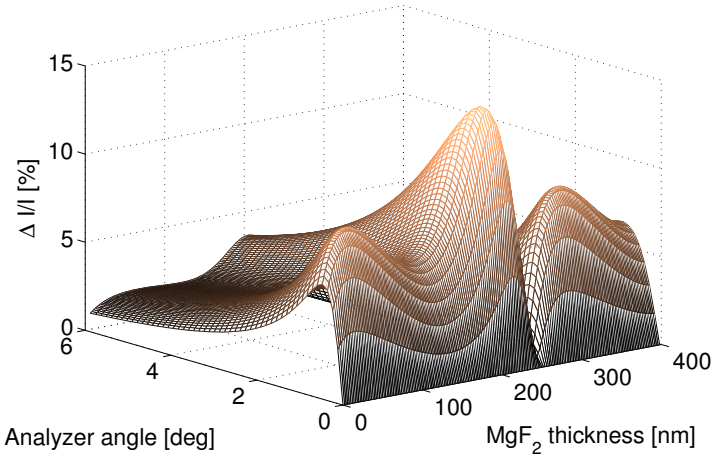

Figure B.2: Modelled signal contrast $\Delta I/I_{av}$ for S-polarized incident light as a function of analyzer angle and MgF_2 thickness. The magneto-optical layer is a 10 nm thin film of Py, which is coated on top of a variable thickness MgF_2 layer. The substrate is Si, coated with a 100 nm thick reflecting layer of Al. Maximum enhancement is predicted for a MgF_2 thickness of 210 nm.

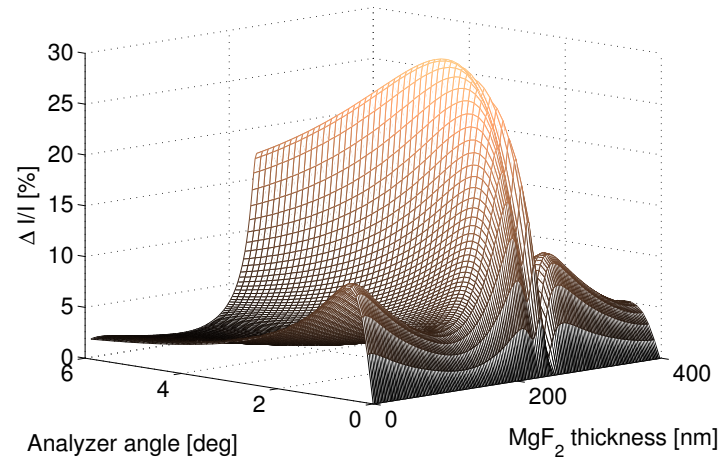

Figure B.3: Modelled signal contrast $\Delta I/I_{av}$ for S-polarized incident light as a function of analyzer angle and MgF_2 thickness. The magnetic layer is a 10 nm thin film of permalloy. A dielectric underlayer of variable thickness MgF_2 is applied, as well as a 80 nm overcoating of ZnS. The substrate is Si, coated with a 100 nm reflecting layer of Al. Maximum enhancement is predicted for a MgF_2 thickness of 230 nm.

Appendix C

Additional experimental results

C.1 Preliminary samples

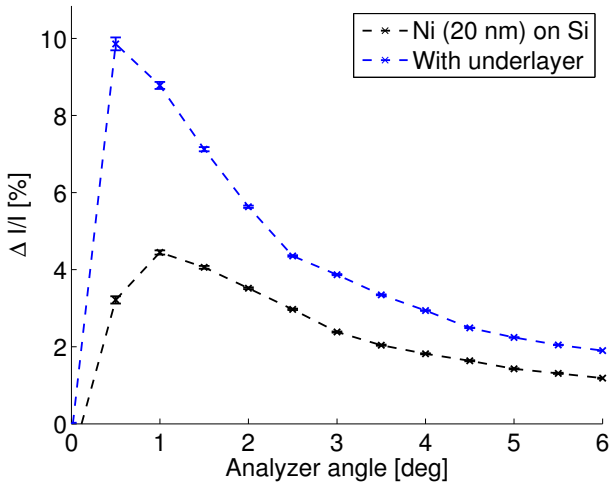

Figure C.1: The signal contrast $\Delta I/I_{av}$ measured for P-polarized incident light on the trilayered sample 1. The sample is a 20 nm thick layer of Ni coated with a variable thickness MgF_2 layer. The substrate is Si (100) coated with 5 nm Cr + 100 nm Au reflecting layer. The results are compared to experimental values from a bare 20 nm thin film of Ni on Si. Note that the analyzer angles are read manually and without higher precision for small angles, and that the dielectric thickness was not measured.

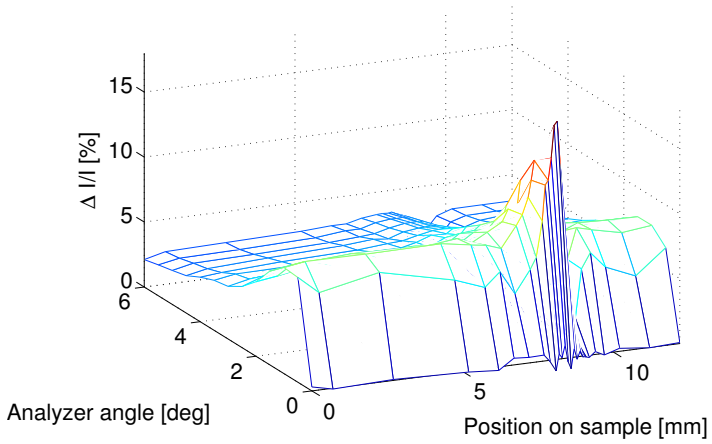

Figure C.2: Measured signal contrast $\Delta I/I_{av}$ for P-polarized incident light as a function of the analyzer angle and position on the sample for the trilayered sample 2. The multilayer configuration is a 20 nm Py thin film deposited on a variable thickness MgF_2 layer. The substrate is Si (100) coated with 100 nm Al. The analyzer angles are read manually and without higher precision for small angles. The dielectric thickness was not measured.

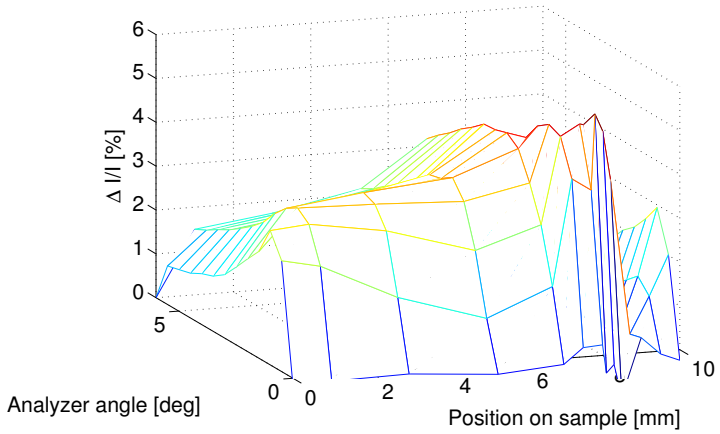

Figure C.3: Measured signal contrast $\Delta I/I_{av}$ for P-polarized incident light as a function of the analyzer angle and position on the sample for the trilayered sample 3. The multilayer configuration is a 10 nm Ni thin film deposited on a variable thickness MgF_2 layer. The substrate is Si (100) coated with 100 nm Al. The analyzer angles are read manually and without higher precision for small angles. The dielectric thickness was not measured.

C.2 Main samples S-polarized light

C.2.1 Sample 4 trilayer configuration

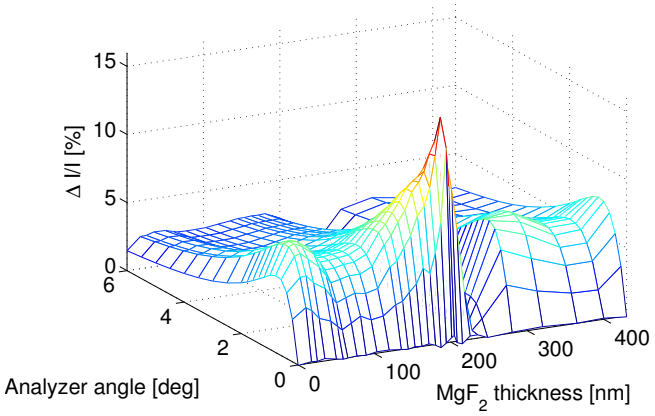

Figure C.4: Measured signal contrast $\Delta I/I_{av}$ for S-polarized light as a function of the analyzer angle and the MgF_2 thickness. The sample is trilayered, with a Si (100) substrate, a 140 nm Al reflective coating, a gradient layer of MgF_2, and finally a 10 nm thin film of Py. Maximum enhancement is observed for a MgF_2 thickness of 205 nm.

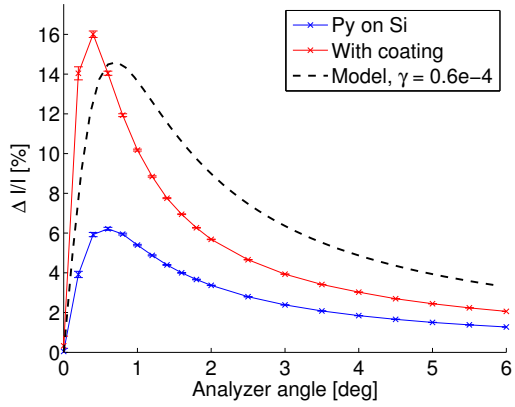

Figure C.5: Maximum measured signal contrast $\Delta I/I_{av}$ for S-polarized incident light as a function of analyzer angle on the trilayered sample 4. The experimental data are compared for a bare Py film on Si and an underlayer of approximately 205 nm MgF_2. The modelled results for S-polarized light with $\gamma = 0.6 \times 10^{-4}$ are also included.

C.2.2 Sample 5 ZnS overlayer

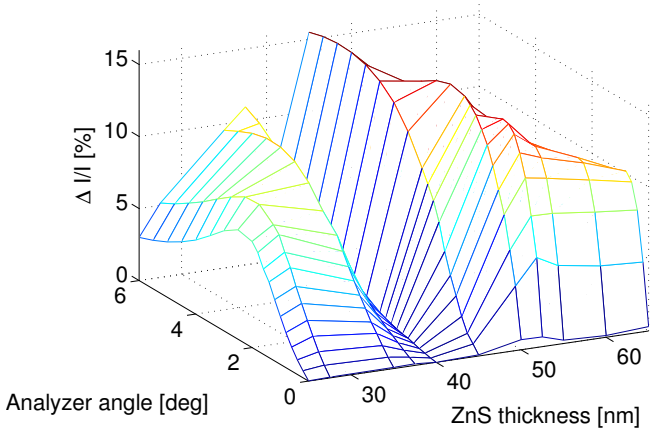

Figure C.6: Measured signal contrast $\Delta I/I_{av}$ without quarter-wave plate for S-polarized incident light as a function of analyzer angle and ZnS thickness. The sample is 10 nm Py overcoated with ZnS. The substrate is Si (100) with 140 nm Al overcoating. Thickness measurements suggest also a 20 nm underlayer of MgF_2. The zero at 40 nm ZnS is due to the Kerr rotation angle θ_k being zero at this configuration.

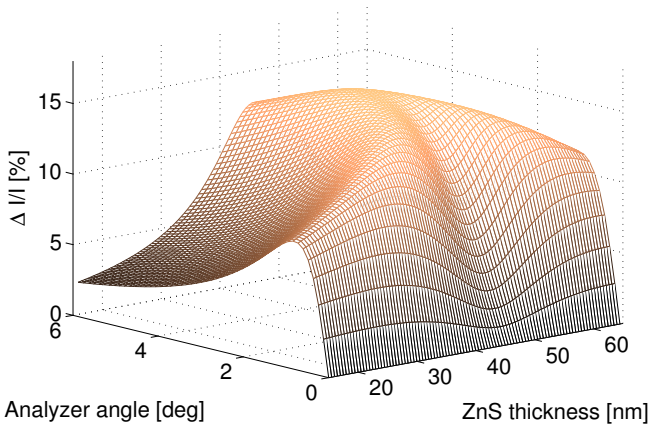

Figure C.7: Modelled signal contrast $\Delta I/I_{av}$ for S-polarized incident light as a function of analyzer angle and ZnS thickness for a quadrilayered system. The configuration is 10 nm Py overcoated with ZnS. The substrate is Si, with 140 nm Al overcoat. A 20 nm thick underlayer of MgF_2 is added in the model to match the experimental situation.

C.2.3 Sample 5 quadrilayer configuration

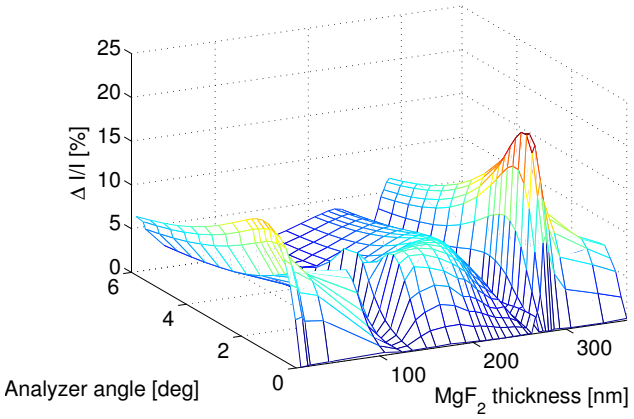

Figure C.8: Measured signal contrast $\Delta I/I_{av}$ without quarter-wave plate for S-polarized light as a function of analyzer angle and MgF_2 thickness. The sample is a Si substrate covered with 140 nm Al, a gradient thickness MgF_2 layer, 10 nm Py, and finally a ZnS coating of approximately 53 nm. The maximum signal contrast of 21.09% is found for a MgF_2 thickness of 284 nm. The zero at a MgF_2 thickness of approximately 120 nm is believed to be due to the Kerr rotation angle being zero at this configuration.

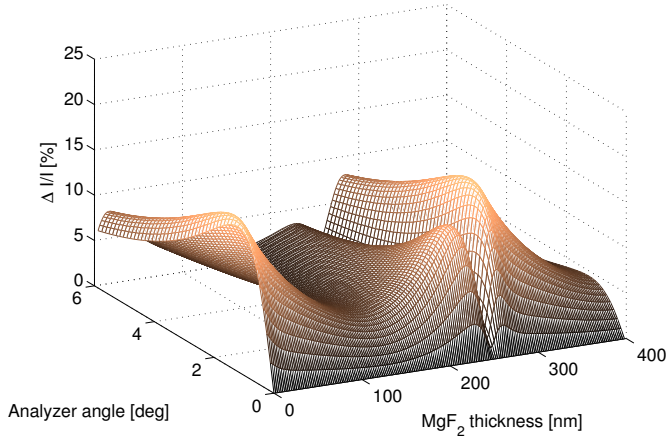

Figure C.9: Modelled signal contrast $\Delta I/I_{av}$ for S-polarized light as a function of analyzer angle and MgF_2 thickness. The configuration is a 10 nm Py with a 53 nm ZnS overcoating and a variable thickness MgF_2 underlayer. The substrate is Si, with a 140 nm Al overcoating.

C.3 Reproducibility test sample

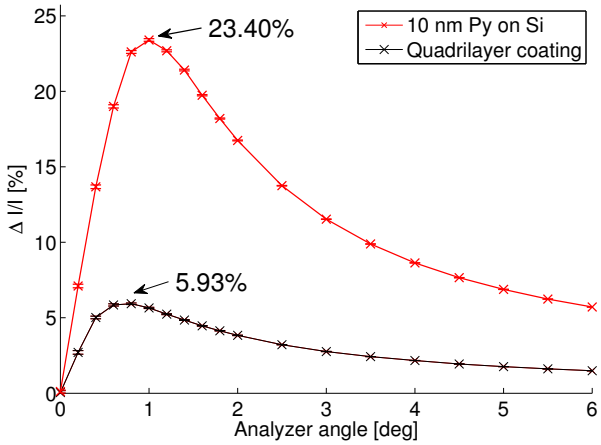

Figure C.10: Measured signal contrast $\Delta I/I_{av}$ for P-polarized light as a function of analyzer angle for the reproducibility test sample 6. The multilayer configuration is a 10 nm thin film of Py enclosed between a variable thickness ZnS overcoat and a variable thickness MgF_2 underlayer. The substrate is Si, with a 2 nm Cr + 80 nm Au reflective layer. The enhancement factor, measured without a quarter-wave plate, is seen to reach 3.95 at the position on the sample with the largest observed signal contrast. The dielectric coating thicknesses were not measured for this sample.

Appendix D

Error considerations

D.1 Note on intensity readout

In the manual of the NanoMOKE^{TM}2 experimental table the manufacturer dissuades measuring longitudinal MOKE when the intensity read by the photodetector is above 4000 mV or below 900 mV. This is because the photovoltage measured by the detector is not linearly proportional to the actual laser intensity outside these ranges. A large quantity of the measurements done in this experiment is outside this photodetector range set by the manufacturer. However, the nonlinearity of the photodetector is not believed to be a problem in this particular experiment, since the actual signal intensity is not an important factor. The figure of interest is the signal contrast $\Delta I/I_{av}$, which is believed to be largely unaffected by photodetector nonlinearity.

It should be noted, though, that some measurements are made at low photodetector intensities. Fig. D.1 shows an example of a hysteresis curve for ϕ =0.2° from the trilayered sample 4: 10 nm permalloy with an approximate 205 nm magnesium fluoride underlayer on a 140 nm aluminium reflective base layer. The low intensity will cause higher uncertainties, though as long as the signal contrast $\Delta I/I_{av}$ is clearly defined, the nonlinearity of the photodetector is not believed to be a source of error.

As discussed in Sec. 4.2.4, a method was implemented for high precision analyzer angle determination based on the asymptotic way the photodetector intensity scales for small angles. The intensity readout scales with the analyzer angle as $I_{av} = a\sin^2\phi + b$ (Eq. 4.1)[8], where a and b are constants to be determined at each position on the sample. In this project, a and b were determined from the measured intensity at the null-intensity $\phi = 0°$, and at 4° off the null-intensity angle. The range of analyzer angles could then be calculated directly from Eq. 4.1.

[8]From the manual of the NanoMOKE 2 instrument.

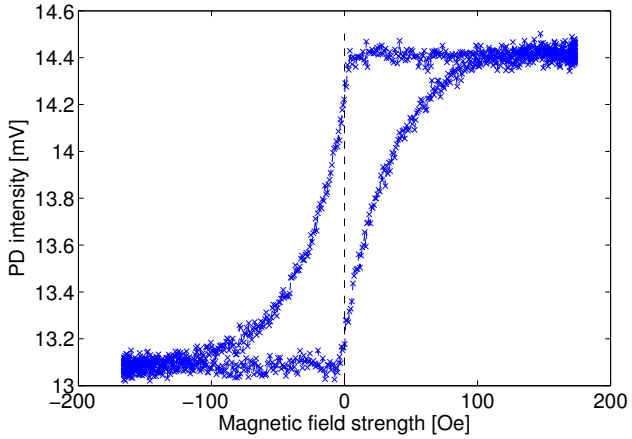

Figure D.1: Hysteresis curve from 10 nm of permalloy on a MgF_2 undercoating where the Fresnel component of the light has almost vanished. Here the signal contrast is large, though the uncertainty in the measurement will be high.

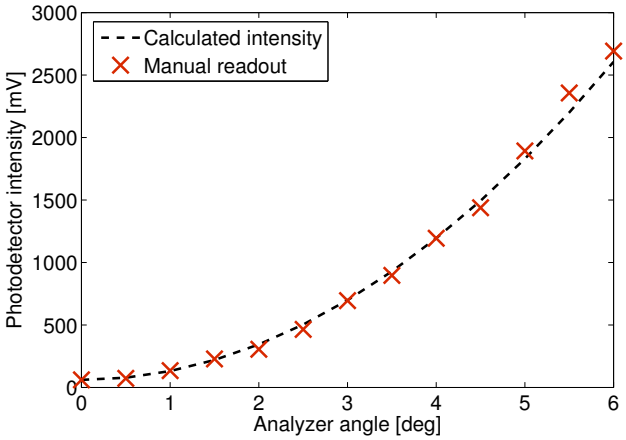

Figure D.2: Photodetector intensities from manual analyzer angle readout are compared to calculated values. The sample is a trilayered sample with 20 nm Py on a MgF_2 underlayer. Note that the manual reading at 0° and 4° define the estimated intensity curve.

Before introducing this method, the analyzer angle was read manually from the polarization analyzer rotator. Fig. D.2 compares manual readout to estimated intensity values for a trilayered sample. It can be seen that the manual intensity readouts follow the calculated asymptotic form, with small deviations. Estimating the pho-

todetector intensity for each angle is believed to give the highest precision of the two methods, especially at small angles, where the figure of interest $\Delta I/I_{av}$ is most sensitive to angle change.

Both the null-intensity and the 4° measurement have uncertainties, though. By estimating an uncertainty in the 4° angle readout of ±0.2°, and an uncertainty in the null-intensity reading of approximately ±1%, the transferred resulting uncertainty for an estimated analyzer angle of 1° is approximately ±0.05°. This is a much higher precision than can be achieved by manual readout of the angle from the polarization analyzer rotator.

D.2 Thickness determination

Measurements of the dielectric thickness gradients were performed with a Tencor Alphastep© 100 analog profilometer. The measured thin film edge thicknesses are read manually from a graph paper with scalebars like the one presented in Fig. D.3. The uncertainties in the measurements are estimated from the fluctuations observed at a presumably flat surface, and must therefore be considered approximate.

Figure D.3: Example of a ZnS film thickness determination made with the analog Tencor Alphastep© 100 profilometer. The scalebar to the right gives thickness in tens of nanometres. The uncertainty in each measurement is estimated from the fluctuations seen at a presumably flat surface, on both sides of the edge.

D.3 Magneto-optical coupling

The amount of Kerr rotation in light reflected off a magnetic thin film is directly linked to the magnitude of the off-diagonal elements of the permittivity tensor, given in Eq. 2.30. Both for nickel and permalloy the off-diagonal elements are difficult to determine experimentally. Visnovsky et al. [46] show how the complex permittivity of nickel, iron, and cobalt vary as a function of the wavelength of the incident light. Five different measurement series are compared, with drastic variations in results, especially for the real part of the off-diagonal permittivity element ϵ_{xy}, which takes values from 0.1-0.25 in the case of Ni.

Table D.1 shows different sources for the off-diagonal permittivity element for nickel, iron, and permalloy. The experimental values are usually given as a complex magneto-optical coupling constant, $Q = Q_r + iQ_i$, where the off-diagonal permittivity element is calculated as $\epsilon_{xy} = -N^2 iQ$, with N being the complex refractive index. As can be seen, the values found vary substantially for different source experiments.

Table D.1: Off-diagonal permittivity of Ni, Fe, and $Ni_{84}Fe_{16}$.

Material	Off-diagonal permittivity	Source
Nickel	(0.1→0.25) - 0.04i	Visnovsky et al . 1993 [46].
Iron	0.7 - 0.25i	Krinchik et al. 1968 [63].
Iron	0.3 - 0.11i	Neuber et al. 2003 [64].
Permalloy	0.2 - 0.08i	Berger et al. 1997 [47]
Permalloy	0.17 - 0.045i	Neuber et al. 2003 [64]
Permalloy	(0.15→0.3) - (0.04→0.06)i	Effective medium approximation.

A method of calculating the off-diagonal permittivity element of permalloy was also tested: A generalized *effective medium approximation* gives the permittivity element of permalloy from the off-diagonal permittivity elements of nickel ϵ_{Ni} and iron ϵ_{Fe} through the relation

$$\epsilon_{Py} = \epsilon_{Ni} + \frac{c(\epsilon_{Fe} - \epsilon_{Ni})}{1 + (1-c)(\epsilon_{Fe} - \epsilon_{Ni})/3\epsilon_{Ni}} \text{ [65]} \tag{D.1}$$

where c is the amount of Fe in the alloy. The values calculated from the effective medium approach does not account for a change in crystal structure causing different

optical behaviour for the alloy and its components, and can only be used as an approximate calculation. The values calculated for permalloy also show large variation depending on the input permittivities of Ni and Fe used.

Whereas the depolarization factor γ can be varied to influence the shape of the $\Delta I/I_{av}$ curve for small angles, it is largely unimportant at larger angles, where the value of the off-diagonal permittivity element ϵ_{xy} is of more importance. The experimental signal contrast curve at large analyzer angles from bare Py on Si was therefore used to fit the value of the off-diagonal permittivity element.

Fig. D.4 shows the experimental curve for 10 nm Py on Si and two different model curves. As can be seen, the best fit value was found in the upper region of the values calculated by the effective medium approach. Possible reasons for this high value can be that the composition of nickel and iron in the permalloy changed from the initial 84:16 to a higher proportion of Fe when the material was evaporated, or that the experimental thickness of the Py film is considerably larger than 10 nm. The latter is not considered very probable, since both AFM and profilometer measurements suggest a thickness of approximately 10 nm Py.

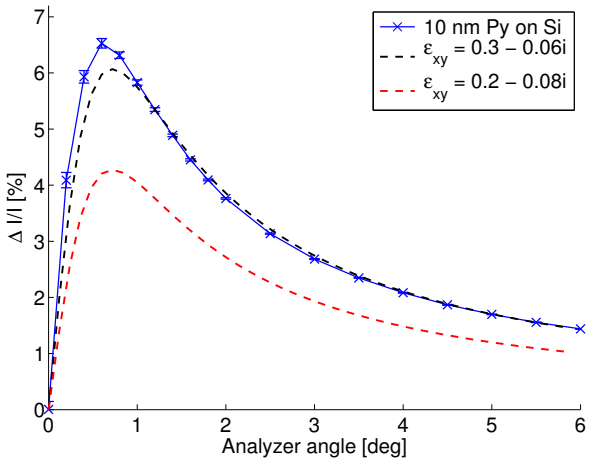

Figure D.4: The off-diagonal permittivity element ϵ_{xy} was fitted to the experimental signal contrast curve of 10 nm bare permalloy on a silicon substrate. The value reported by Berger et al. [47] is seen to give a modelled signal contrast that is significantly lower than the experimental results.